Power uprates
and plant life extension

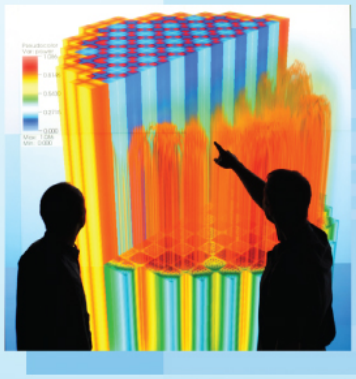

Engineering design
and analysis

Science-enabling
high performance
computing

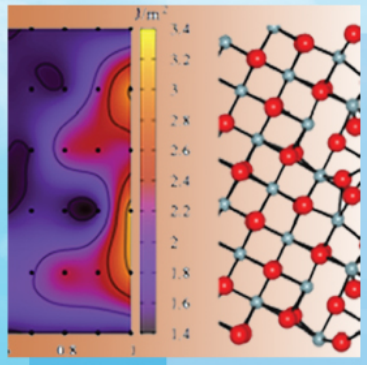

Fundamental science

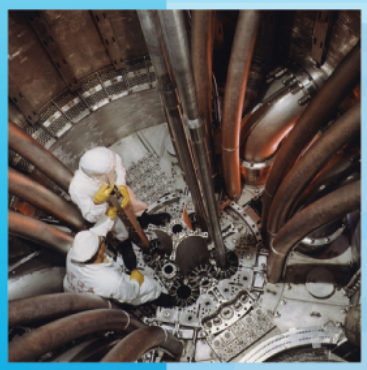

Plant operational data

Consortium for Advanced Simulation of LWRs

# CASL-U-2013-0140-000

A.Guion, G. Rabello dos Anjos,
C. Narayanan, J. Buogiorno,
MIT, ASCOMP

June 2013

U.S. DEPARTMENT OF ENERGY | Nuclear Energy

# Closure Relation for Microlayer Evaporation in Nucleate Boiling, and its Application to ITM Test Case 3b

A. Guion[1], G. Rabello dos Anjos[1], C. Narayanan[2], J. Buongiorno[1*]

[1] Massachusetts Institute of Technology, Cambridge, MA, USA
[2] ASCOMP GmbH, Zurich, Switzerland
* jacopo@mit.edu

(Rev. 1)

Massachusetts Institute of Technology
Cambridge, MA, USA
June 2013



CASL-U-2013-0140-000

## Abstract

*The phase change model in the code TransAT was tested for the case of a vapor bubble growing in an infinite superheated liquid, for which an analytical solution (Scriven solution) exists. Water (both at atmospheric pressure and PWR conditions), refrigerants R134a and HFE-7100, and fictitious fluids with more favorable properties were tested. The initial set of simulations was conducted with the reference diffuse-interface, 2D axisymmetric approach available in the code. The results are in qualitative agreement, but also have large quantitative discrepancy with respect to the analytical solution, with no convergence upon mesh refinement. Therefore, during the course of the project a new sharp-interface 2D axisymmetric treatment of the energy equation in TransAT was developed/tested, and finally applied to the Scriven bubble cases. The sharp-interface treatment greatly improves the quality of the phase change model, which now reproduces the analytical solution very accurately, with 2$^{nd}$ order convergence upon mesh refinement.*

*A model for the evaporation of the microlayer underneath a bubble growing at the wall was developed. The model assumes conduction heat transfer through the microlayer, evaporation at the liquid/vapor interface with no thermal resistance at the interface, and no flow within the microlayer. The model was implemented in a user-defined routine written in C++ in TransAT, so it can be used as a subgrid model in the simulation of bubbles near walls.*

*Finally, nucleate boiling of a single bubble at a heated wall (Test Case 3b) was simulated with the sharp-interface treatment, with and without the microlayer subgrid model. Comparison to the ad-hoc experimental database generated for CASL in FY12 indicates that the simulations are capable of capturing the bubble evolution, shape and size correctly, including the bubble departure diameter. However, the bubble departure time predicted by the simulations is significantly higher than that observed experimentally.*

## Contents

Abstract ..... 2

1 Bubble Growth in Superheated Liquid Simulated using TransAT's Reference Diffuse-Interface Approach ..... 4

1.1 Refrigerant HFE-7100 ..... 6

1.2 Refrigerant R134a ..... 8

1.3 Atmospheric Water ..... 9

1.4 Pressurized Water Reactor – PWR ..... 11

2 Benchmark Simulations with TransAT's Advanced Sharp-Interface Approach ..... 13

2.1 Stefan Problem ..... 14

2.1.1 Problem Formulation ..... 14

2.1.2 Numerical Simulations and Results ..... 15

2.2 Sucking Interface Problem ..... 16

2.2.1 Problem Formulation ..... 16

2.2.2 Numerical Simulations and Results ..... 18

2.3 Bubble growth in infinite superheated liquid (Scriven Bubble) ..... 20

2.3.1 Fictitious fluid case ..... 20

2.3.2 Growth of steam bubble in water ..... 23

2.4 Summary ..... 23

3 Microlayer Evaporation Subgrid Model ..... 25

4 Growth and detachment of a single steam bubble from a wall at saturated pool boiling conditions (Test Case 3b) ..... 29

4.1 Problem Formulation ..... 29

4.2 Numerical Simulations and Results ..... 30

4.2.1 Simulations with constant wall superheat ..... 31

4.2.2 Simulations with conjugate heat transfer ..... 34

4.2.3 Simulations with micro-layer model ..... 37

5 Conclusions and future work ..... 37

References ..... 38

APPENDIX – C++ routines for implementation of the microlayer subgrid model in TransAT ..... 39

In FY13 the focus of the Interface Tracking Methods (ITM) work at MIT and Ascomp was on the phase change models in the *TransAT* code, and in particular resolution of several issues which had been identified in previous years. This report describes the FY13 efforts. Briefly, a series of benchmark simulations for a single spherical bubble growing within an infinite superheated liquid were performed first with the reference diffuse-interface treatment of the energy equation available in *TransAT* (Section 1). Major improvements in accuracy and computational cost were possible with the development of an advanced sharp-interface treatment of the energy equation, which is described in Section 2. A model to capture the evaporation of the microlayer was developed and implemented into a user-defined function for use as a subgrid phase change model (Section 3). The new phase change models were then applied to the simulation of a single bubble growing at a heated wall, or Test Case 3b (Section 4).

# 1 Bubble Growth in Superheated Liquid Simulated using TransAT's Reference Diffuse-Interface Approach

The mass transfer (or evaporation) model in the reference level-set formulation of *TransAT* was first tested by simulating the growth of a spherical vapor bubble in an infinitely extended superheated liquid for various working fluids. This test case aims at assessing the accuracy of the implemented mass transfer model while neglecting the effects of gravity, conjugate heat transfer and forced flow. The bubble growth process may be viewed as occurring in two basic stages, according to (Plesset & Zwick , 1954). The very first stage, also called inertial-controlled growth, is governed by the momentum interaction between the superheated liquid and the bubble itself, in which temperature and pressure are at the highest values. Later, the second stage is reached when the temperature and pressure inside the bubble are at the lowest values and the bubble's growth is limited by heat transport taking place within the superheated liquid. Such a stage is called heat-transfer-controlled growth. If viscous and surface tension effects are neglected, an exact solution can be used to compare the numerical simulation to the second stage of the bubble growth process. The exact solution was obtained by (Scriven, 1959) by considering the interface at the saturation temperature and it has been used by several authors for validation of their numerical codes. The solution is given in the form of the bubble radius $r$ as a function of time t as:

$$r(t) = 2\beta\sqrt{\gamma_l t} \tag{1}$$

where $\gamma_l$ is the liquid thermal diffusivity and $\beta$ is a growth constant which can be found in (Scriven, 1959), and depends on the properties of the fluid and the liquid superheat. In order to simulate the second stage of bubble growth with the right initial conditions, a thin thermal boundary layer must be placed on the liquid side. The initial temperature field can be found from (Scriven, 1959) as a function of the spatial coordinate $r$ and time $t$. The thermal boundary layer thickness $\delta_T$ is defined as the distance form the interface to the point in the liquid where 99% of the temperature difference has occurred:

$$\delta_T = r\big(T = T_{sat} + 0.99 * (T_\infty - T_{sat})\big) - r_0 \tag{2}$$

where $T_{sat}$ is the saturation temperature, $T_\infty$ is the temperature in the bulk of the fluid and $r_0$ is the initial bubble radius. The temperature profile given by Eq. (2) is fitted through a parabolic curve for the sake of simplicity. Note that due to the thin thermal boundary layer, the computational grid must be dense where the temperature gradient is high in order to predict the heat and mass fluxes correctly at the interface.

Three fluids were selected for the simulations, namely refrigerants HFE-7100, R134a and water, so that we are able to compare the solutions predicted by the numerical simulations to their correspondent analytical solution and to the numerical simulations found in (Magnini , 2012), for a range of the fluid properties. Water was simulated at atmospheric pressure, while the saturation pressure of refrigerants R134a and HFE-7100 was set at $84kPa$ and $52kPa$ , respectively. A summary of the fluid properties in the liquid and vapor phases is presented in Table (1). Density is represented by $\rho$, viscosity by $\mu$, heat capacity by $c_p$ and thermal diffusivity by $\varphi$. Surface tension, latent heat of vaporization and pressure are respectively denoted by $\sigma$, $h_{lv}$ and $p$. The bubble growth constant $\beta$ was calculated from the equations given in (Scriven, 1959) and its value is $\beta = 15.11$ for water, $\beta = 17.1$ for HFE-7100 and $\beta = 9.32$ for refrigerant R134a. The initial thermal boundary layer thickness $\delta_T$ was set to $7\mu m$ for water, $5.8\mu m$ for HFE-7100 and $11.4\mu m$ for the refrigerant R134a.

Figure (1) shows a comparison of the continuous, discrete and analytical thermal boundary layer for R134a, which presents the thickest boundary layer of all the fluids tested. For a uniform grid of $401x201$ points, only 2 points are within the boundary layer. For a grid of $601x301$ points, the number of points is increased to 3 and, finally, for a grid of $801x401$ points, 4 points are used to discretize the thermal boundary layer. Note that for any point inside the bubble, the temperature is $T = T_{sat}$ and for those points in the liquid phase outside the thermal boundary layer $\delta_T$, the temperature is $T = T_\infty$.

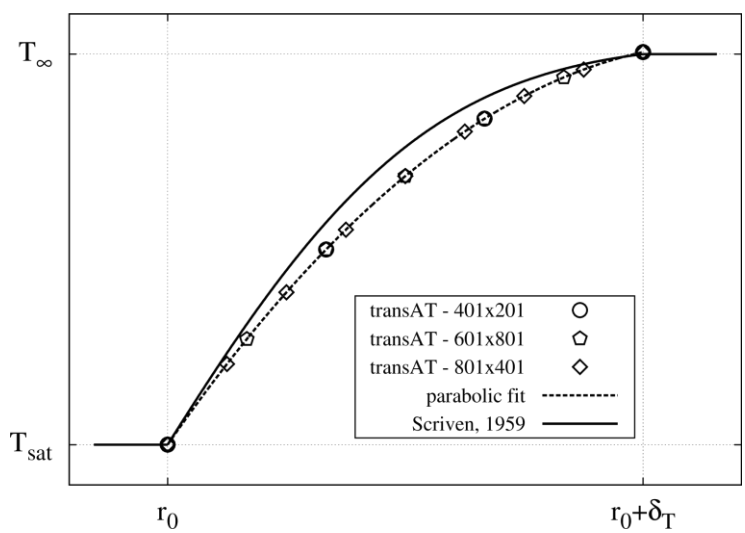


Figure 1 Continuous, discrete and analytical thermal boundary layers for the bubble growth test case.

The computational grid is an important parameter to accurately address the simulation of the physical problem. The thin thermal boundary layer requires a dense set of points next to the interface in order to compute the mass flux $j_v$ with accuracy. Moreover, the computational domain should be sufficiently large to accommodate the vapor bubble expansion without creating edge effects. Figure (2) shows a detailed sketch of the domain geometry, the boundary conditions applied to the bubble growth problem and the initial conditions used to simulate the test cases presented in this report. Due to the symmetric nature of the problem, the simulations were performed using an axisymmetric geometry. The initial bubble radius was set at $r_0 = 0.1mm$, the length and height of the domain were $4r_0 = 0.4mm$ and $8r_0 = 0.8mm$, respectively. The outlet pressure condition is imposed at all boundaries, except in

$X = X_{min}$, in which the symmetry condition was imposed. The vapor is at saturation temperature $T = T_{sat}$, and the initial superheated liquid temperature is increased by 5 degrees Kelvin, i.e. $T_l = T_{sat} + 5K$. Three different grid refinement levels were used to verity convergence, namely $401x201$, $601x301$ and $801x401$ grid points. The first number represents the grid in the $X$ direction, while the second represents the $Y$ direction. Similar test cases can be found in (Kunkelmann & Stephan , 2009 ) and (Magnini , 2012); the latter will be compared to the numerical solution obtained by our simulations using *TransAT*. All the simulations presented in this section were performed in a 12-core machine with Intel Xeon processor running at $2.93GHz$ and with $24Gb$ of RAM memory. However the numerical code usage was limited to 4-cores per simulation.

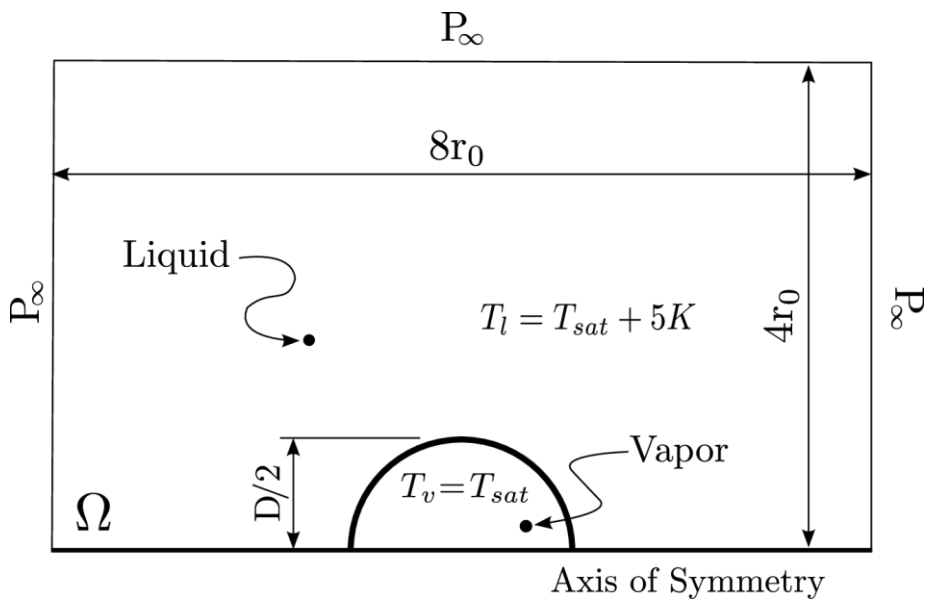


Figure 2 Schematic representation of the domain geometry, the boundary conditions applied to the bubble growth problem and the initial conditions used to simulate an axisymmetric bubble growth. The vapor bubble is located at the center of the axis boundary.

## 1.1 Refrigerant HFE-7100

The first test case is for the refrigerant HFE-7100. Figure (3) shows a comparison with three different grid refinement levels used in *TransAT*, the analytical solution given by (Scriven, 1959) and a numerical solution found in (Magnini , 2012), which was generated with the commercial software *Fluent* to simulate the growth of an axisymmetric bubble with the same conditions of our test. As can be seen, the numerical solutions given by *TransAT* under predicts the analytical solution for the three presented grids, however for $t < 1.5ms$ using a $601x301$points grid, the solution is overpredicted. The same behaviour is found in the commercial code *Fluent* where the analytical solution is underpredicted for time $t < 2ms$ and it approaches the analytical solution for time $t > 2ms$. Note that the shape of all the *TransAT* and *Fluent* simulations is flat, which suggests that the thickness of thermal boundary layer is approximately constant, contrary to the expected thickening of the boundary layer with time.

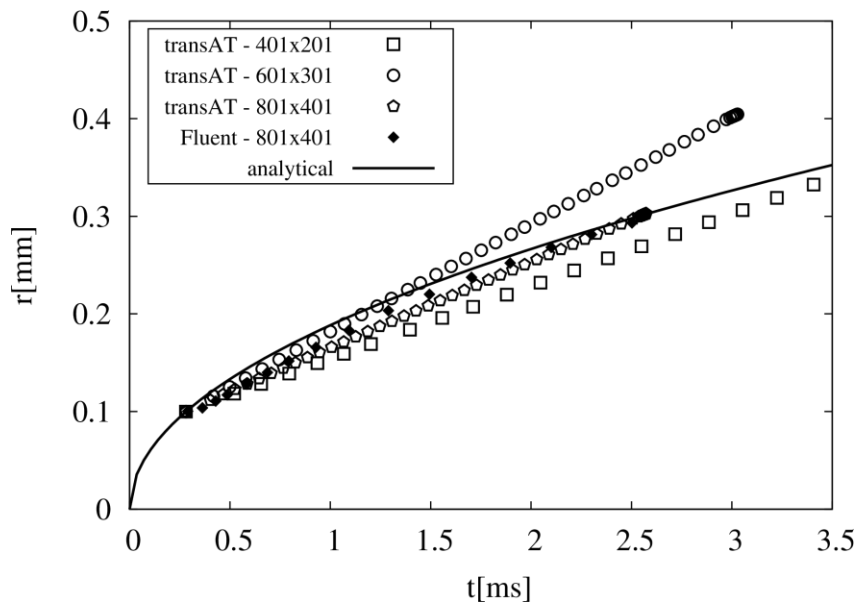


Figure 3 Comparison of three grid refinement levels using the commercial software *transAT*, the analytical solution presented by (Scriven, 1959) and the numerical solution found in (Magnini , 2012) through the commercial software *Fluent* for refrigerant HFE-7100.

Figure (4) shows temperature snapshots at three different time steps for the Cartesian grid of $601x301$. In Fig. (4a) the initial condition is shown for the bubble growth test case. The blue color represents the saturation temperature, which was set to $T_{sat} = 314.15K$, and due to the initial conditions, the superheated temperature was, consequently, set to $T = 319.15K$. As can be seen, the spherical shape of the vapor bubble is not preserved during the numerical simulation, where interface irregularities can be noticed at the top of the vapor bubble for time $t = 0.881ms$. Additionally, the temperature of the vapor phase is not maintained constant at the saturation temperature, which is unphysical. To complete the simulations for this test case, 3 days were required for the coarsest grid, while the most refined grid required approximately 10 days of computation.

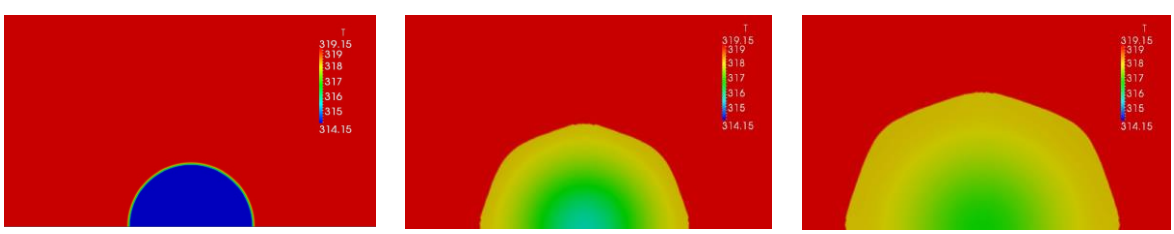


(a) (b) (c)

Figure 4 Vapor bubble shape and temperature field in a superheated liquid (HFE-7100). The Cartesian grid was set to $\mathbf{601x301}$ points and the simulation time corresponds to (a) $\boldsymbol{t = 0.000ms}$, (b) $\boldsymbol{t = 0.881ms}$ and (c) $\boldsymbol{t = 1.346ms}$.

## 1.2 Refrigerant R134a

The simulations of the refrigerant R134a are presented in this section. Figure (5) shows a comparison of three different grid refinement levels used in the axisymmetric simulation of the vapor bubble growth in *transAT*, the analytical solution given by (Scriven, 1959) and the numerical solution found in (Magnini , 2012) for axisymmetric simulation on *Fluent*. The linear growth was again found for the three numerical grids herein presented and the solution did not converge upon mesh refinement. Moreover, the grid used in the *Fluent* simulation presented better results for the same number of points in *TransAT*, where the curve overpredicts the analytical solution.

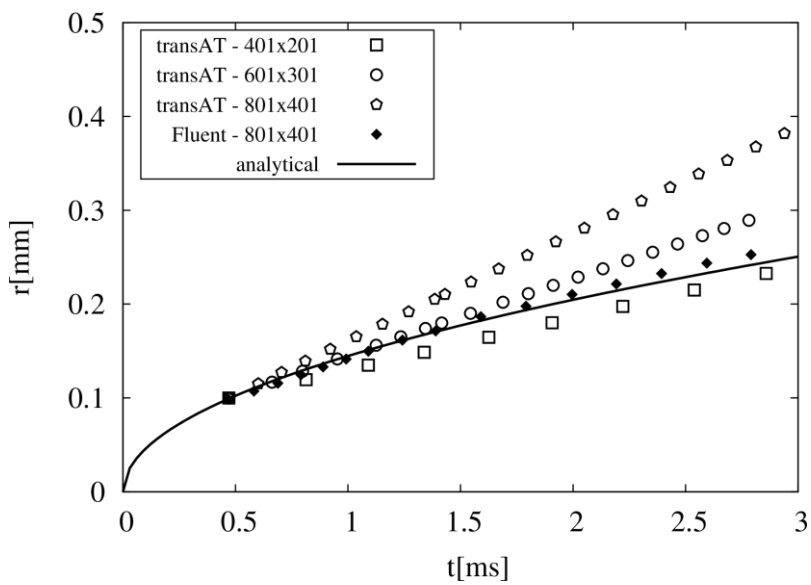


Figure 5 Comparison of three grid refinement levels using *TransAT*, the analytical solution presented by (Scriven, 1959) and the *Fluent* numerical solution found in (Magnini , 2012) for refrigerant R134a.

Figure (6) shows three snapshot of the temperature field of the refrigerant R134a for three different time steps using a Cartesian grid of $601x301$ points. The initial temperature for the vapor bubble and the superheated liquid is shown in Fig. (6a). The blue color represents the saturation temperature, which was set to $T = 243.15K$ and the superheated temperature was set to $T = 248.15K$. As can be seen, the spherical shape of the bubble is not preserved during the numerical simulation, where interface irregularities can be noted at the top of the vapor bubble and next to the symmetry axis for time $t = 1.032ms$. It is noticeable a gradient of the temperature field in the vapor phase, which does not agree with the expected constant saturation temperature in the vapor. The simulations presented in this section were carried out approximately in 2, 5 and 9 days for the $401x201$, $601x301$ and $801x401$grid points respectively.

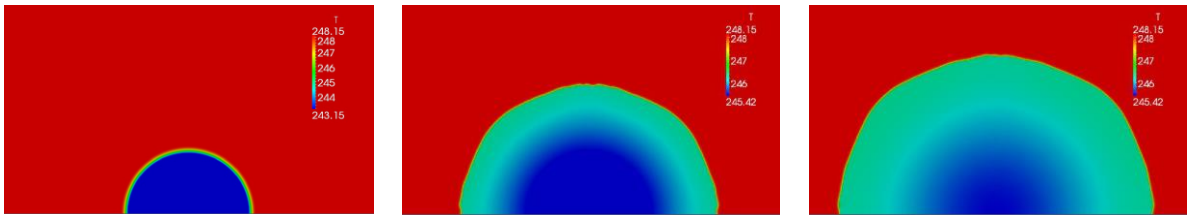


(a) (b) (c)

Figure 6 Vapor bubble shape and temperature field in a superheated liquid (R134a). The Cartesian grid was set to $\boldsymbol{601x301}$ points and the simulation time corresponds to (a) $\boldsymbol{t = 0.000ms}$, (b) $\boldsymbol{t = 1.032ms}$ and (c) $\boldsymbol{t = 1.453ms}$.

## 1.3 Atmospheric Water

Water is used at high pressure in pressurized water reactors (PWR) and boiling water reactors (BWR). However, for this first water simulation, the fluid properties at atmospheric pressure were used, as shown in Table (1). Figure (7) shows a comparison of the numerical solution of given by *transAT* for three different grids, the analytical solution from (Scriven, 1959) and the numerical solution found in (Magnini , 2012). It was found that the numerical results for the three grids tested in the simulation of water vapor bubble growth presented divergence from the analytical solution, where a larger bubble growth rate is noticed for the grids $601x301$ and $801x401$. The solution did not converge upon mesh refinement. It is important to note that the mass transfer implementation in *Fluent* was developed in (Magnini , 2012) as an additional algorithm through the user defined functions (UDF), and it is not part of the standard algorithms available in the commercial package.

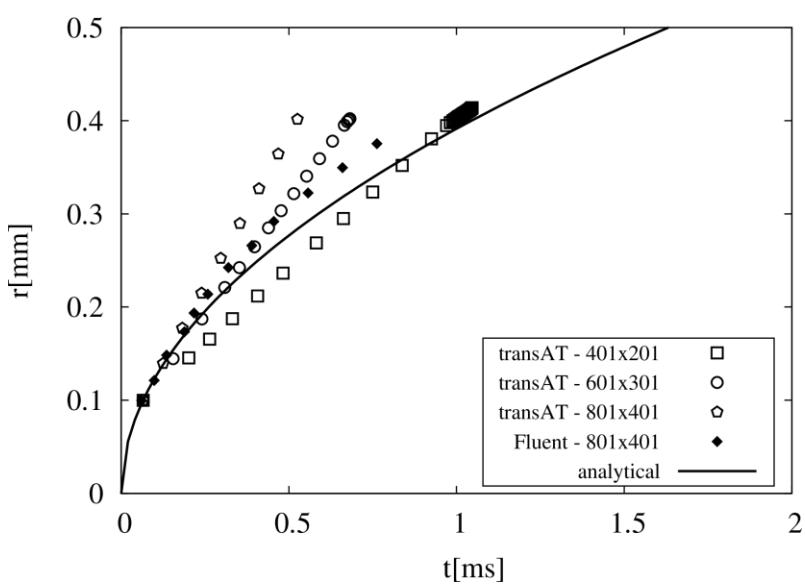


Figure 7 Comparison of three grid refinement levels using the commercial software *transAT*, the analytical solution presented by (Scriven, 1959) and the numerical solution found in (Magnini , 2012) through the commercial software *Fluent* for water as working fluid.

The evolution of the shape and temperature field with time for a water vapor bubble growth in a superheated liquid is presented in Fig. (8) for three different snapshots in time $t = 0.000ms$, $t = 0.381ms$ and $t = 0.433ms$. As seen in the previous test cases, the spherical shape of the vapor bubble is not preserved the same interface irregularities were found for three grid refinement levels and the temperature in the vapor phase is different from the expected saturation temperature. The simulations presented in this section were carried out approximately in 6, 7 and 8.5 days for $401x201$, $601x301$and $801x401$grid points respectively.

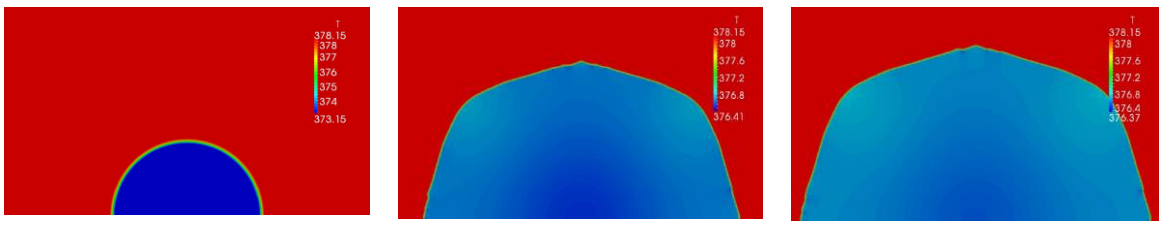


(a) (b) (c)

Figure 8 Vapor bubble shape and temperature field in a superheated liquid (water at atmospheric pressure). The figures are for the Cartesian grid $\boldsymbol{601x301}$ points and the simulation time corresponds to (a) $\boldsymbol{t = 0.000ms}$, (b) $\boldsymbol{t = 0.381ms}$ and (c) $\boldsymbol{t = 0.433ms}$.

Table 1 Fluid properties used in the numerical simulations with TransAT.

| Property | HFE-7100 | | R134a | | Water | |
|---|---|---|---|---|---|---|
| | Liquid | Vapor | Liquid | Vapor | Liquid | Vapor |
| $\boldsymbol{\rho[kg/m^3]}$ | 1425 | 5.15 | 1388 | 4.43 | 958 | 0.597 |
| $\boldsymbol{\mu[\mu Pa \cdot s]}$ | 356 | 11.13 | 401 | 9.64 | 277 | 12.55 |
| $\boldsymbol{c_p[kJ/kg \cdot K]}$ | 1.43 | 0.9 | 1.27 | 0.72 | 4.22 | 2.03 |
| $\boldsymbol{\gamma[mW/m \cdot K]}$ | 61.8 | 10.3 | 106 | 9 | 679 | 25 |
| $\boldsymbol{\sigma[mN/m]}$ | 13.6 | | 16 | | 59 | |
| $\boldsymbol{h_{lv}[kJ/kg]}$ | 117.8 | | 219.5 | | 2257 | |
| $\boldsymbol{T_{sat}[K]}$ | 314.15 | | 243.15 | | 373.15 | |
| $\boldsymbol{p[kPa]}$ | 52 | | 84 | | 100 | |

## 1.4 Pressurized Water Reactor – PWR

Subcooled flow boiling occurs in the hot subchannel(s), typically starting past the core midplane. Because of the high pressure and low surface tension of water at PWR conditions, the bubbles generated at the wall and then entrained by the subcooled liquid tend to be small, order of $100\mu m$ and below. For such a condition, the relevant fluid properties are described in Table 2. The simulation of a single bubble growth is analyzed at the PWR conditions. The superheated temperature is again set to be $T_l = T_{sat} + 5K$, therefore $T = 622.85K$. The bubble radius and the domain size are kept unchanged from the previous test cases. For the proposed PWR conditions the growth constant is $\beta = 0.539$, which is one order of magnitude lower then the previous benchmarks, therefore slow bubble growth is expected for the numerical simulations.

Table 2 Fluid properties used in the numerical simulations with TransAT for water at PWR condition

| Property | Water at PWR | |
|---|---|---|
| | Liquid | Vapor |
| $\boldsymbol{\rho[kg/m^3]}$ | 595 | 101 |
| $\boldsymbol{\mu[\mu Pa \cdot s]}$ | 73 | 23 |
| $\boldsymbol{c_p[kJ/kg \cdot K]}$ | 9.1 | 13.7 |
| $\boldsymbol{\gamma[mW/m \cdot K]}$ | 448 | 123 |
| $\boldsymbol{\sigma[mN/m]}$ | 4.8 | |
| $\boldsymbol{h_{lv}[kJ/kg]}$ | 965 | |
| $\boldsymbol{T_{sat}[K]}$ | 617.82 | |
| $\boldsymbol{p[kPa]}$ | 15.51 | |

Figure 9 shows a comparison of 2 grid refinement levels using *TransAT* and the analytical solution of (Scriven, 1959). The numerical solution under predicts the analytical solution, and the same flat shape observed in the previous section is seen here. Moreover, it was noticeable that little difference exists between the results from the two grids.

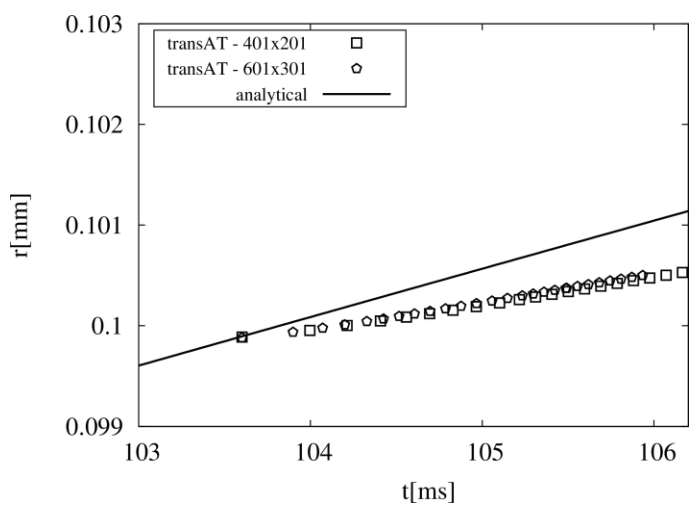


(a)

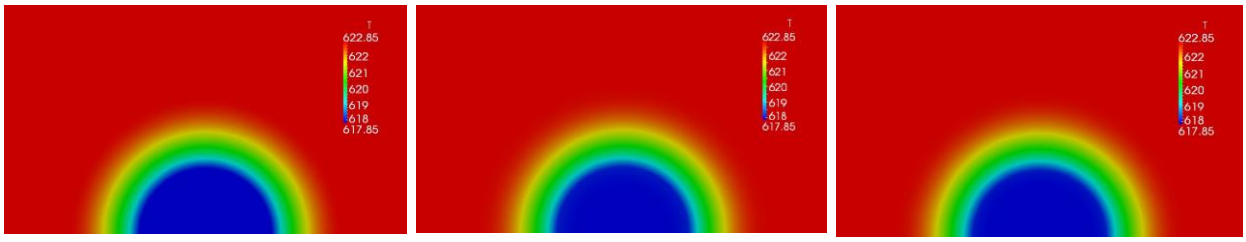


(b) (c) (d)

Figure 9 (a) Bubble radius history for bubble at PWR conditions. Evolution of the vapor bubble shape and temperature field with time vapor bubble growth in a superheated liquid for water at PWR condition. The Cartesian grid was set to $601x301$ points and the snapshots were taken in the simulation time (b) $t = 0.000ms$, (c) $t = 103.6ms$ and (d) $t$ =105.9ms

Snapshots of the shape and temperature for the PWR bubble are shown in Figure 9b-d. Again, we note that the saturation temperature is not maintained at the saturation value within the vapor phase. Surface irregularities similar to those from the previous sections were not observed for the PWR bubble simulations. These simulations were carried out approximately in 3 and 4 days for $401x201$ and $601x301$ grid points respectively.

In summary, the simulations performed with the diffuse-interface approach revealed some issues: (i) unphysical linear growth of the bubbles, (ii) unphysical deviation of the vapor temperature from the saturation temperature, (iii) surface irregularities at the interface, and (iv) no convergence upon mesh refinement. These behaviors were attributed to under-resolution of the thermal boundary layer in the diffuse-interface approach (i and iv), as well as possibly incorrect implementation of the saturation temperature boundary condition at the vapor/liquid interface (ii and iv), and implementation of the curvature/surface tension model in the diffuse-interface approach (iii). To overcome these problems, it was decided to develop a sharp-interface formulation for the energy equation, which is the equation where the temperature gradient is resolved and the evaporation rate determined. The results for the sharp-interface approach are presented in the following section.

# 2 Benchmark Simulations with TransAT's Advanced Sharp-Interface Approach

The phase change modeling in TransAT was originally implemented as a first-order relaxation model. It was found that this method was enough to solve simple problems such as the Stefan problem; however, it required very fine resolution to match the analytical solution for the Sucking Interface problem. Essentially for the cases with strong phase change under conditions of large density ratios between the vapor and the liquid and very low thermal diffusivity, the thermal boundary layer resolution requirement is very stringent. Second-order modeling of the heat flux at the interface is necessary to get grid convergence at reasonable resolutions (as shown in the section on the sucking interface problem below).

The energy jump condition across the vapor-liquid interface is given as,

$$j_v h_{fg} = -\sum_{k=1}^{2} q_j^k n_j^k \tag{3}$$

Where, $j_v$ is the phase change rate, $h_{fg}$ is the latent heat of vaporization, $q_j^k n_j^k$ is the heat flux entering the interface from the side of phase $k$ and $n_j^k$ is the outward pointing normal to the phase. The main challenge is the calculation (modeling) of the net heat flux entering the interface.

In the reference approach in TransAT a *first-order heat-flux model (diffuse interfacial heat-flux model)* based on relaxation of the interface temperature to $T_{sat}$ is implemented as follows,

$$\sum_{k=1}^{2} q_j^k n_j^k = \sum_{k=1}^{2} \lambda_k (T^k - T_{sat}) \delta^I \tag{4}$$

Where $\lambda$ is the thermal conductivity, $T^k$ is the phase temperature and $\delta^I$is the Dirac delta function at the interface. For a single temperature model, this simplifies to,

$$\sum_{k=1}^{2} q_j^k n_j^k = (\lambda_g + \lambda_l)(T - T_{sat}) \delta^I \tag{5}$$

Note that in this model the interface temperature is not exactly $T_{sat}$ but tends to it on grid refinement with a first-order convergence behavior.

In the course of this study, the heat-flux model was improved to a second-order method. The second-order heat-flux model (*sharp interfacial heat-flux model*) is based on the work of Gibou et al. (2007). The interface temperature is assumed to be $T_{sat}$ through the use of the Ghost Fluid Method of Fedkiw et al. (1999). The heat flux is calculated from both sides of the interface through extrapolation of the temperature on to the ghost cells with the assumption that the interface temperature is equal to $T_{sat}$.

The new sharp-interface phase-change model was validated for simple one-dimensional and axisymmetric problems before application to the nucleate boiling problem (Section 4). The following problems were simulated for validation:

- Stefan problem: One-dimensional with constant density
- Sucking Interface problem: One-dimensional with large density ratio and thin thermal boundary layers
- Bubble growth in infinite medium: Scriven (reference) bubble growth

Details follow.

## 2.1 Stefan Problem

The problem described here is the one-dimensional problem in (Hardt and Wondra, 2008; Welch and Wilson, 2000).

### 2.1.1 Problem Formulation

Both the liquid and the vapor phases are considered incompressible and are initially in quiescent equilibrium. Heat is transferred by conduction from a flat, solid, isothermal surface to the adjacent vapor that in turn experiences an increase in temperature and a thermal profile develops in the vapor driving evaporation of the liquid at the vapor/liquid interface. The vapor is considered motionless but the liquid is pushed away from the solid boundary with the interface also moving in the same direction. It is also assumed that the moving interface remains flat so that the problem can indeed be seen as one-dimensional. Under these assumptions, there exists a closed-form analytical solution to this problem. Briefly, the liquid temperature profile is uniform and the energy equation in the vapor phase can be expressed as follows:

$$\frac{\partial T}{\partial t} = \alpha \frac{\partial^2 T}{\partial x^2}, \qquad 0 \le x \le \delta(t) \tag{6}$$

where $\delta(t)$ is the coordinate of the interface position. $\alpha$ is the thermal diffusivity of the vapor phase ($\alpha = \lambda / \rho c_p$). The boundary conditions of the problem are:

$$\begin{aligned} T\left(x = \delta(t), t\right) &= T_{sat} \\ T\left(x = 0, t\right) &= T_{wall} \end{aligned} \tag{7}$$

and the jump condition at the interface is the following:

$$\rho_g v_{\text{int}} h_{f\,\text{g}} = -\lambda_g \left.\frac{\partial T}{\partial x}\right|_{x=\delta(t)} \tag{8}$$

$\rho_g$ is the density of the vapor, $v_{\text{int}}$ is the interface velocity, $h_{f\,\text{g}}$ is the latent heat of vaporization and $\lambda_g$ is the thermal conductivity of vapor. The analytical solution to this problem is given by (Alexiades and Solomon, 1993) and (Gupta, 2003)

$$\begin{aligned} \delta(t) &= 2\beta\sqrt{\alpha t} \\ T(x,t) &= T_{wall} + \left(\frac{T_{sat} - T_{wall}}{erf(\beta)}\right) erf\left(\frac{x}{2\sqrt{\alpha t}}\right) \end{aligned} \tag{9}$$

with $erf(x)$ being the error function and $\beta$ being a solution to the following equation:

$$\beta \exp\left(\beta^2\right) erf(\beta) = \frac{c_p\left(T_{wall} - T_{sat}\right)}{h_{l\,\text{g}}\sqrt{\pi}} \tag{10}$$

A schematic representation of the Stefan problem simulated here is given in Figure 10.

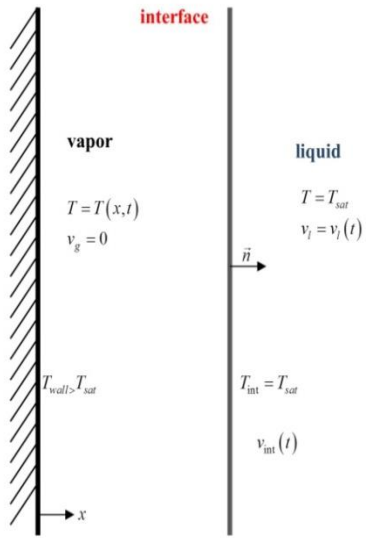


Figure 10. Domain schematic representation for Stefan problem

### 2.1.2 **Numerical Simulations and Results**

The simulations, conducted using the code TransAT, are one-dimensional. The computational domain is bounded by two walls both sustained at a constant temperature. The domain size is $x$=1 mm.

$$\begin{aligned} T(x=0,t) &= 383.15\ K \\ T(x=1,t) &= 373.15\ K \end{aligned} \tag{11}$$

The temperature everywhere in the domain is initialized as $T(x,t=0)=T_{sat}$. The properties of the working fluids can be seen in Table 21. Note that two different vapor thermal conductivity values (0.1 and 0.01 W/m K as in Hardt and Wondra, 2008) were explored. A grid independence analysis is also conducted using three different spatial resolutions for both conductivity cases. A uniform grid is employed in all our simulations. The discretization details for the simulated cases are presented in Table 2.

Table 2. Working fluid properties for Stefan Problem simulations with TransAT

| **Properties** | **Liquid** | **Vapor** |
|---|---|---|
| $\rho\ (kg/m^3)$ | 1 | 1 |
| $\mu\ (Pa\,s)$ | 0.01 | 1e-5 |
| $\lambda\ (W/mK)$ | 1 | 0.1 or 0.01 |
| $c_p\ (J/kgK)$ | 1000 | 1000 |
| $h_{lg}\ (kJ/kg)$ | 1000 | |
| $\sigma\ (N/m)$ | 0.01 | |
| $T_{sat}$ | 373.15 | |
| $T_{wall}$ | 383.15 | |

Table 3. Discretization parameters for the Stefan problem

| $\lambda_g$=0.01W/mK and $\lambda_g$=0.1W/mK | |
|---|---|
| *Grid* | *dx (μm)* |
| *1* | 15.625 |
| *2* | 7.810 |
| *3* | 3.910 |

The spatial schemes used for the convective and viscous fluxes and for the advection of the Level Set function are HLPA (2nd order) and Quick (3rd order) respectively. The scheme employed for time marching is the Euler (1st order). These schemes are used in all subsequent simulations. Figure 11 shows the interface position as a function of time. The numerical results converge to the analytical solution upon mesh refinement.

For the Stephan problem, grid converged and accurate results were obtained for the first-order phase change model. Results for the second-order method are not presented in this report.

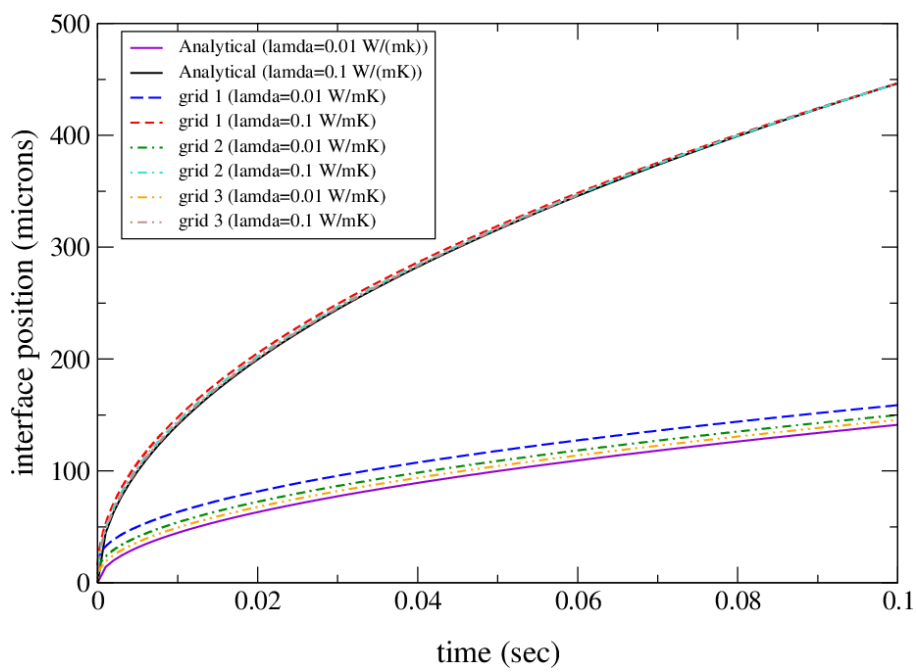


Figure 11. Interface position for Stefan problem as simulated with TransAT for different spatial resolutions and different conductivities. The analytical solution is also plotted for comparison.

## 2.2 Sucking Interface Problem

The problem described here is the one-dimensional problem in (Welch and Wilson, 2000; Sato and Niceno, 2011).

### 2.2.1 Problem Formulation

Again, a one-dimensional flow is considered with both the liquid and the vapor phases being incompressible. In this case though, the vapor is at uniform saturation temperature, while the liquid phase is superheated, thus is in a metastable state at a distance extending beyond the interface. A schematic

representation of the sucking interface problem simulated here is given in Figure 12. This problem is planar equivalent of the Scriven bubble discussed in Section 3. Note that this problem is a stringent test case due to the large density ratio between steam and water and the low thermal diffusivity of water.

The situation described here, results in the formation of a thin thermal boundary layer in the liquid that is moving with the interface. The thermal layer will tend to remain thin as its diffusive spreading is counteracted by the sucking of the layer towards the interface. The following transformation of the spatial coordinate can be made:

$$\xi = x - \int_0^t v_{\text{int}}(t)\,dt \tag{12}$$

With the transformation of equation **Error! Reference source not found.** the coordinate $\xi$ is such that the interface is located at $\xi = 0$. Then, the energy equation in the liquid phase can be transformed into the following:

$$\frac{\partial T}{\partial t} + \left(v - v_{\text{int}}\right)\frac{\partial T}{\partial \xi} = \alpha \frac{\partial^2 T}{\partial \xi^2} \tag{13}$$

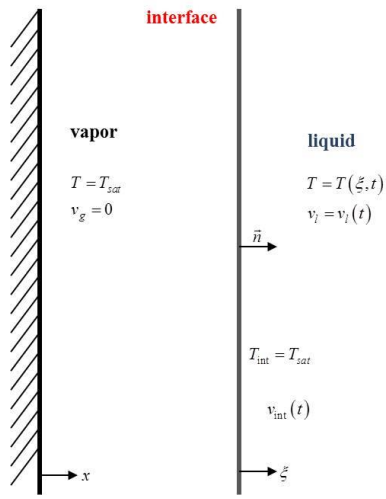


Figure 12. Domain schematic representation for the sucking interface problem

The boundary and initial conditions are the following:

$$\begin{aligned} T(\xi = 0, t) &= T_{sat} \\ T(\xi \to \infty, t) &= T_o \\ T(\xi, t = 0) &= T_o \end{aligned} \tag{14}$$

where $T_o$ is the liquid temperature in the bulk phase and $T_{sat}$ is the saturation temperature. The jump conditions across the interface can be seen here:

$$\rho\left(v_l - v_{\text{int}}\right)h_{lg} = -\lambda \left.\frac{\partial^2 T}{\partial \xi^2}\right|_{\xi=0} \tag{15}$$

$$-\rho_g v_{\text{int}} = \rho\left(v_{\text{int}} - v_l\right) \tag{16}$$

The problem is reduced to a simplified equation by using the jump conditions and by defining the following constants:

$$B = \frac{\alpha}{C\beta},\ \beta = \frac{\rho_g}{\rho_l},\ C = \frac{\lambda}{\rho_g h_{\mathrm{lg}}} \tag{17}$$

The new equation is as follows:

$$\frac{\partial T}{\partial t} - \beta v_{\mathrm{int}} \frac{\partial T}{\partial \xi} = \alpha \frac{\partial^2 T}{\partial \xi^2} \tag{18}$$

In which the interface velocity is given by

$$v_{\mathrm{int}} = C \left. \frac{\partial T}{\partial \xi} \right|_{\xi=0} \tag{19}$$

Then, by introducing the parameter $\eta = \sqrt{\frac{1}{2\alpha}} \frac{\xi}{\sqrt{t}}$ and by implementing the transformation

$$T(x,t) = B\phi(\eta) \tag{20}$$

one arrives to the ordinary differential equation that defines the similarity solution for this problem:

$$\phi'' + \left(\eta + \phi'(0)\right)\phi' = 0 \tag{21}$$

with its transformed boundary conditions:

$$\begin{aligned} B\phi(\eta = 0) &= T_{sat} \\ B\phi(\eta \to 0) &= T_o \end{aligned} \tag{22}$$

The solution to the non-linear differential equation (21) was used for the purpose of comparison with TransAT results.

### 2.2.2 Numerical Simulations and Results

The simulations conducted using TransAT are one-dimensional. The domain size is $x$=8 mm and it is defined by a wall on one side and an open boundary on the other side. The temperature in the vapor region of the domain is initialized as $T(x,t=0) = T_{sat}$. The liquid region is superheated with a degree of superheat of 5 K. The initial thermal boundary thickness is 0.476 mm and the interface is initially placed at 0.3 mm. The simulation starts from 0.1 s of the analytical solution. The working fluids are water and vapor at saturation pressure of 1 atm. The properties can be seen in Table 4. A grid independence analysis is also conducted. A uniform grid is employed in all our simulations. The initial interface thickness is captured by 2.5, 10, 38 and 76 cells respectively. The discretization details are presented in

Table 5.

Table 4. Working fluid properties for sucking interface problem simulations with TransAT

| **Properties** | **Water** | **Vapor** |
|---|---|---|
| $\rho\ (kg/m^3)$ | 958 | 0.579 |
| $\mu\ (Pa\,s)$ | 0.00028 | 1.26e-5 |
| $\lambda\ (W/mK)$ | 0.679 | 0.025 |
| $c_p\ (J/kgK)$ | 4220 | 2030 |
| $h_{lg}\ (J/kg)$ | 2.26e+6 | |
| $T_{sat}\ (K)$ | 373.15 | |

Table 5. Discretization parameters for the sucking interface problem

| Grid | dx (μm) | Initial boundary layer resolution |
|---|---|---|
| 1 | 200 | 2.4 |
| 2 | 50 | 9.5 |
| 3 | 12.5 | 38 |
| 4 | 6.25 | 76 |

Figure 13 shows the interface position as a function of time for the first-order method. The numerical results converge to the analytical solution upon mesh refinement. Note that the resolution requirement for the first-order method is very high with the initial thermal boundary layer being resolved with 76 grid cells.

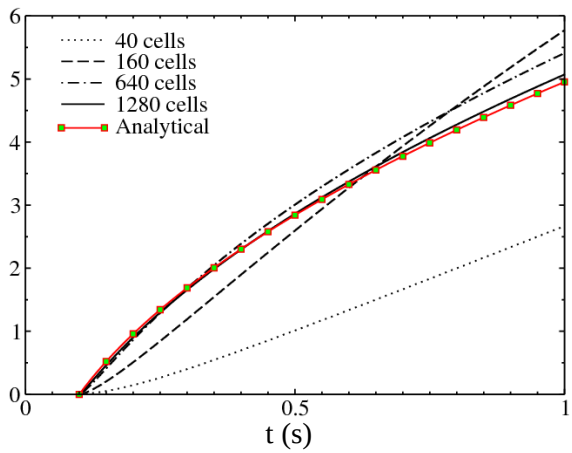


Figure 13. Interface position (in mm) for sucking interface problem as simulated with TransAT for different spatial discretizations. The similarity solution is also plotted for comparison.

Simulation results with the sharp-interface (second-order) model are shown in Figure 14 below. It can be seen that with the sharp-interface model much coarser grids are sufficient to give grid-convergent and accurate results. In particular the Grid 2 used for the first-order method is already sufficient – implying approximately 10 points inside the initial thermal boundary layer.

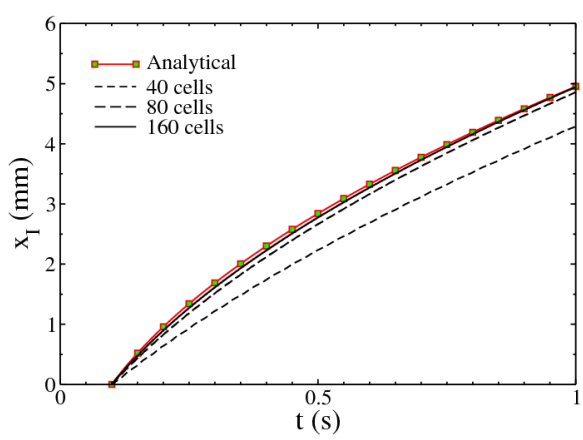


Figure 14. Interface position for sucking interface problem as simulated with TransAT for different spatial discretizations. The similarity solution is also plotted for comparison.

The results from the sucking interface problem clearly show that for the cases with thin thermal boundary layers forming at the interface, the diffuse-interface first-order heat-flux model requires too high resolution making it practically unusable. The sharp-interface second-order method on the other hand converges rapidly to the analytical solution.

## 2.3 Bubble growth in infinite superheated liquid (Scriven Bubble)

The problem presented here is the same described in Section 1 above. In our analysis we start the simulation assuming that the bubble has an initial radius $R_o$. By using the Scriven equations one can compute the time at which the bubble has this radius as well as the initial thermal boundary layer thickness at the bubble-liquid interface.

For our simulations, we are using again the code TransAT and both spherically symmetric and axisymmetric simulations were performed. For the axi-symmetric simulations a part of the bubble corresponding to an angle of 1 rad was simulated.

Due to the fact that water has a very thin thermal boundary layer (~10μm) requiring very high resolution, we start our simulations by using a fictitious fluid of high thermal diffusivity and low latent heat as a first test. Then, the case of water and steam is also simulated. The simulation domain for both cases can be seen in Figure . The size of the domain is different for the two different cases examined here. The boundary conditions as well as the initial conditions are the same in both cases. The boundary conditions can also be seen in Figure .

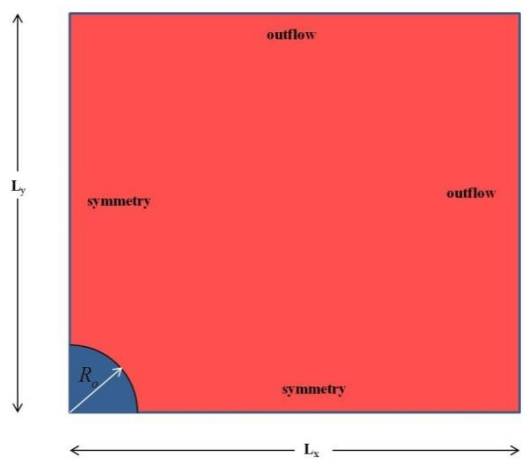


Figure 15. Computational domain and boundary conditions for the bubble growth in infinite medium problem.

### 2.3.1 Fictitious fluid case

The properties of the liquid and the vapor used for this series of simulations can be seen in **Error! eference source not found.**. The domain size is $L_x$=$L_y$=6 mm. Several different grid resolutions have been used and the details can be seen in Table 5. Working fluid properties for fictitious fluid bubble growth simulations with TransAT

| Properties | Liquid | Gas |
|---|---|---|
| $\rho\ (kg/m^3)$ | 200 | 5 |
| $\mu\ (Pa\,s)$ | 0.1 | 0.005 |
| $\lambda\ (W/mK)$ | 40 | 1 |
| $c_p\ (J/kgK)$ | 400 | 200 |
| $h_{lg}\ (J/kg)$ | 1.0e+5 | |
| $T_{sat}\ (K)$ | 500 | |
| $\Delta T\ (K)$ | 5 | |
| $\sigma\ (N/m)$ | 0.1 | |
| $g\ (m/s^2)$ | 9.81 | |
| $Ro$ (μm) | 100 | |

Table 6 in terms of how many nodes were used to resolve the thermal boundary layer at the gas-liquid interface. In this case, the initial bubble radius is a function of the spatial resolution.

Table 5. Working fluid properties for fictitious fluid bubble growth simulations with TransAT

| Properties | Liquid | Gas |
|---|---|---|
| $\rho\ (kg/m^3)$ | 200 | 5 |
| $\mu\ (Pa\,s)$ | 0.1 | 0.005 |
| $\lambda\ (W/mK)$ | 40 | 1 |
| $c_p\ (J/kgK)$ | 400 | 200 |
| $h_{lg}\ (J/kg)$ | 1.0e+5 | |
| $T_{sat}\ (K)$ | 500 | |
| $\Delta T\ (K)$ | 5 | |
| $\sigma\ (N/m)$ | 0.1 | |
| $g\ (m/s^2)$ | 9.81 | |
| $R_o$ (μm) | 100 | |

Table 6. Grid parameters for the fictitious fluid case

| Grid | Boundary layer resolution (nodes) |
|---|---|
| 1 | 6 |
| 2 | 12 |
| 3 | 24 |
| 3b | 30 |
| 4 | 48 |
| 5 | 96 |

The results for the bubble radius growth for the fictitious fluid with high thermal diffusivity assuming spherical symmetry is shown in Figure 16 for the sharp-interface second-order heat-flux model. Note that in the FY12 version of the report the comparison was made to the Plesset equation – however it turns out that for the low density ratio case considered here the general solution of Scriven (1959) should be taken as reference. The solution converges to the exact solution on grid refinement. A very good match is already obtained for grid size of 80 μm. The simulations with axi-symmetry also give very similar results with grid convergence obtained at around 80 μm resolution. This is shown in Figure 17. Simulations with higher resolutions were not performed for the axi-symmetric cases due to their computational cost and time constraints.

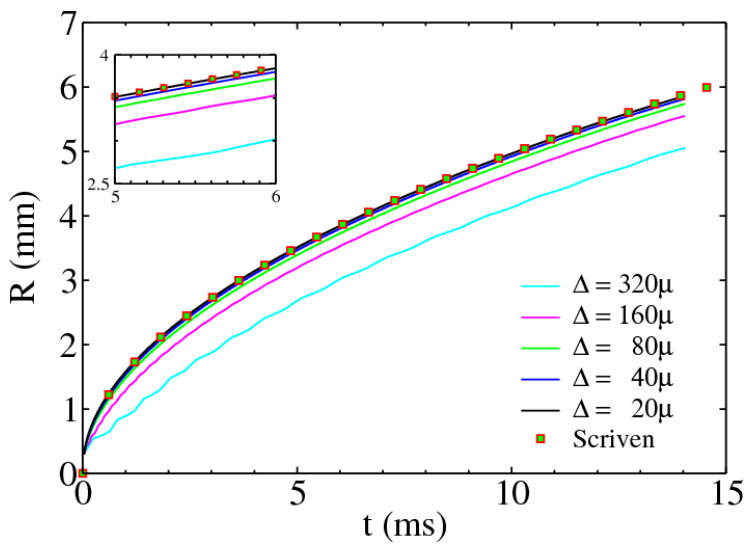


Figure 16. Bubble radius growth with time for the fictitious fluid case. The analytical solution plotted here is Scriven (1959).

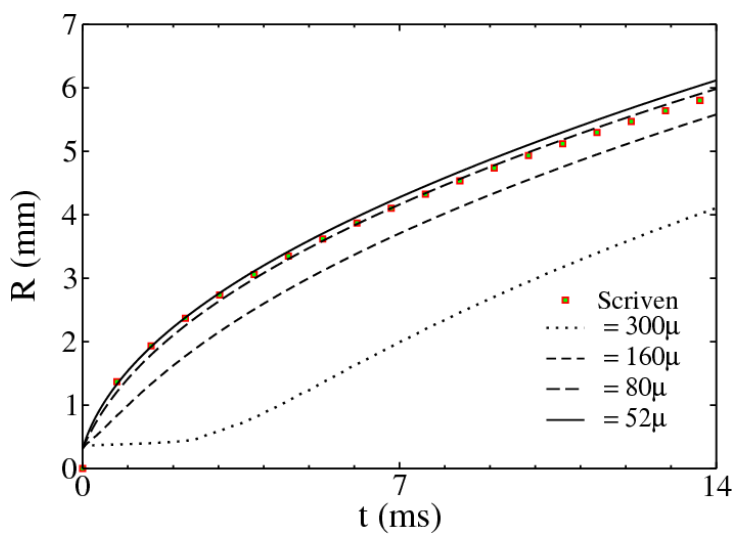


Figure 17. Bubble radius growth with time for the fictitious fluid case, simulated in axi-symmetric. The analytical solution plotted here is Scriven (1959).

### 2.3.2 Growth of steam bubble in water

The properties of the liquid and the gas used for this series of simulations are those for water and steam presented already in Table 4 3 above. The domain size is $L_x$=$L_y$=0.4 mm. Several different grid resolutions have been used and the details can be seen in Table 7. The initial radius in this case is 30μm.

The growth of the bubble as a function of time can be seen in Figure 18 under the assumption of spherical symmetry. The simulations converge to the Scriven/Plesset analytical solution on grid refinement. This is a particularly challenging case given the reasons mentioned before, i.e. high density ratio implying high volume production on evaporation, and low thermal diffusivity of water. Axi-symmetric simulations for the water/steam system have not been performed, since it is expected to give similar results (as shown for the fictitious fluid).

Table 7. Discretization parameters for the water case

| Grid | Grid resolution (μm) |
|---|---|
| 1 | 8 |
| 2 | 4 |
| 3 | 2 |
| 4 | 1 |
| 5 | 0.5 |
| 6 | 0.25 |

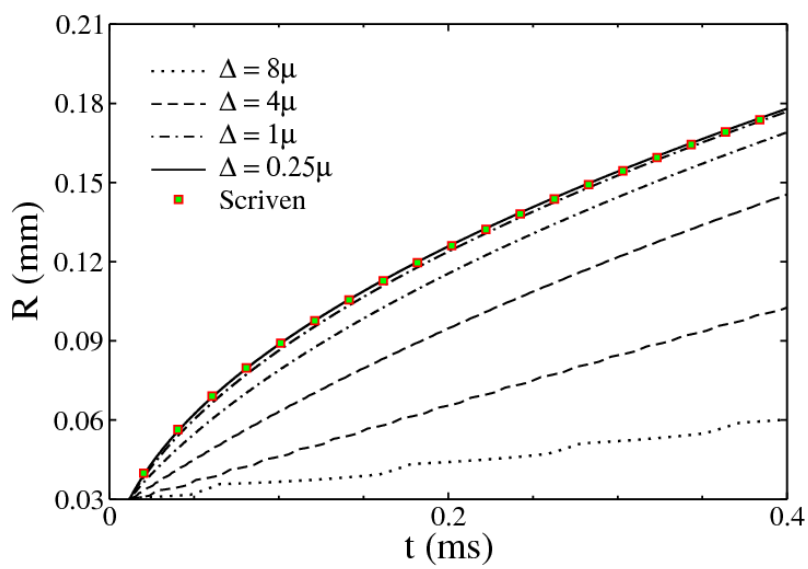


Figure 18. Steam bubble radius as a function of time with comparison between numerical results and analytical solution.

## 2.4 Summary

The new sharp-interface second-order approach implemented in TransAT in FY13 shows good convergence to the analytical solutions of all basic benchmarks examined, including the challenging

Scriven bubble, which could not be reproduced correctly by the older diffuse-interface first-order approach.

# 3 Microlayer Evaporation Subgrid Model

The level-set approach solves an hyperbolic equation in Φ, the signed distance function (the shortest distance to interface) to track the interface on a fixed Eulerian grid. In the presence of mass transfer, source terms appear in the level-set equation, the velocity divergence equation and the energy equation. In *TransAT* the local interfacial mass transfer can be computed either directly from resolution of the temperature gradient and heat flux or via models available which are in the form:

$$\frac{j_v}{u'} = f\left(\frac{Pr}{Sc}, Re_t\right) \tag{23}$$

The contribution from the microlayer underneath a bubble growing at a heated wall would be added through an extra source term calculated from a subgrid model that captures its evaporation at the micro scale.

In the microlayer region, high heat fluxes are achievable due to the small thickness of the microlayer, and once established, microlayer evaporation can contribute significantly to bubble growth. To illustrate this point, if we approximate the microlayer as an axisymmetric wedge of maximum thickness $\delta max$ and radius R then the volume of vapor $V_{ml}$ resulting from complete evaporation of the microlayer is:

$$V_{ml} = \frac{2}{3}\pi R^2\ \delta_{max}\frac{\rho_f}{\rho_g} \tag{24}$$

The ratio to the volume of vapor $V_b$ in the bubble (assume hemispherical) above the microlayer itself:

$$\frac{V_{ml}}{V_b} = \frac{\delta_{max}}{R}\frac{\rho_f}{\rho_g} \tag{25}$$

Assuming typical values of the parameters for a steam bubble at atmospheric pressure ($\delta max \sim 2\mu m$, $R \sim 500\mu m$, $\rho_f$ = 958kg/m$^3$, $\rho_g$ = 0.6kg/m$^3$), $\frac{V_{ml}}{V_b} \sim 6$. Although this estimate greatly over predicts the microlayer contribution (thickness profile is not flat), it suggests there is plenty of liquid in the microlayer to contribute to the growth of the bubble. If the microlayer evaporates completely over a period of time $\tau \sim 5$ms, the average evaporation mass flux from the microlayer can be estimated as:

$$j_v \sim \frac{\rho_g V_{ml}}{\pi R^2 \tau} \sim 0.3\ kg/m^2 s \tag{26}$$

The corresponding local heat flux removed by microlayer evaporation is:

$$q'' \sim j_v h_{fg} \sim 600\ kW/m^2 \tag{27}$$

More realistic orders of magnitude estimates can be obtained from post-processing of experimental measurements of microlayer profiles and steam bubble diameter at atmospheric pressure (Kim and Buongiorno, 2011), which are reported in Table 8 below.

Table 8: Estimates of microlayer contribution to bubble growth, post-processed from the experiments of (Kim and Buongiorno, 2011)

| **time** | **t=1ms** | **t=2ms** | **t=3ms** |
|---|---|---|---|
| $\frac{V_{ml}}{V_b}$ | 0.17 | 0.20 | 0.10 |
| $j_v$ $[kg/m^2s]$ | 0.9 | 1.3 | 1.3 |
| $q''$ $[MW/m^2]$ | 2.0 | 3.0 | 3.0 |

There exist also some theoretical models of microlayer evaporation. Two approaches are found in the literature: (i) the microlayer formation model reported in (Van Carey, 2008), from which an estimate of the microlayer thickness can be obtained which is one order of magnitude above the expected thickness of (1-10um); (ii) in Stephan and Hammer (1994) and Wang et al. (2007), the Reynolds lubrication theory is used to find a steady-flow solution of the microlayer shape, for each time step, leading to growth time consistent with experiments, but inconsistent length scales, i.e. micron-long microlayer instead of hundreds of microns long, as observed experimentally. In CASL we have been developing a new microlayer model that solves for the microlayer thickness as a function of time, distance from bubble root (axisymmetric model) and includes the effect of conjugate heat transfer in the substrate. The model assumes that energy transfer within the microlayer occurs by conduction, there is no thermal resistance at liquid/vapor interface, and there is no lateral flow within the microlayer. A detailed derivation and some limited validation of the model are reported in (Guion et al. 2013); here we give only the governing equation:

$$\frac{\partial \delta}{\partial t} = -\frac{k_l \Delta T}{\rho_f h_{fg} \delta} \tag{28}$$

Where $\delta$ is the microlayer thickness and $\Delta T = T_w - T_{sat}$ is the local wall superheat, which can be solved to find the evolution of the microlayer profile. However, the parameter of interest for the subgrid model is the evaporative mass flux $j_v$ from the microlayer. If $S_k$ is the evaporating surface between a position $r_k$ and a position $r_{k+1}$, then the mass flux becomes:

$$j_{v,k} = \frac{\rho_f}{S_k} \left| \frac{\partial V_{micro,k}}{\partial t} \right| = \frac{\rho_f}{S_k} \frac{\partial}{\partial t} \left[ \int_{[r_k, r_{k+1}]} \delta 2\pi r \, dr \right] \tag{29}$$

Since little information is known about the initial profile, we use a simple linear approximation of it:

$$\delta(r, 0) = \delta_0 + s \times r \tag{30}$$

where $s$ is the initial slope (taken from experiments and typically equal to ~0.01) and $\delta_0$ is the so-called absorbed layer thickness under which the microlayer can no longer evaporate because of long-range (Van Der Walls) molecular forces. $\delta_0$ is orders of nanometers and has no effect on the resolution of the microlayer.

There are two methods to add the contribution from microlayer evaporation to the global bubble growth: (i) compute the evaporative mass flux directly as:

$$j_{v,k} = \frac{k_l \Delta T}{h_{fg} \delta_k} \tag{31}$$

and then integrate the flux over the whole microlayer surface area $S$, or (ii) compute the rate of decrease of the total microlayer volume $\dot{V}_{micro}$ (Eq. 29 integrated over the whole microlayer surface). Both methods are equivalent in meaning, but not in the calculation scheme. The second method is more convenient. To verify that the method is accurate, we tested its performance for the simple case of a constant $\Delta T$ for which an analytical solution of Eq. 28 exists:

$$\delta(r,t) = \left(\delta(0,r)^2 - \frac{2k_l \Delta T}{\rho_f h_{fg}} t\right)^{0.5} \tag{32}$$

which therefore allows for an *analytical* integration of Eq. 31. The *numerical* scheme computes the total microlayer volumes at each time step and then its rate of change during dt:

$$\dot{V}_{micro} = \frac{V_{micro}(t+dt) - V_{micro}(t)}{dt} \tag{33}$$

The figure of merit to evaluate the performance of the numerical method is defined as $\Delta$:

$$\Delta = \frac{j_{v_{analytical}} - j_{v_{numerical}}}{j_{v_{numerical}}} \tag{34}$$

From the upper schemes implementation (trapezoidal rule for integration) we expect a first order convergence of the results, also confirmed by the sensitivity study for time and space discretizations, as reported in Table 9.

Table 9: Effect of time and space discretization on $\Delta$

| Max $\Delta$: | $dr{\sim}12.5nm$ | $dr{\sim}25nm$ | $dr{\sim}50nm$ | $dr{\sim}0.1\mu m$ | $dr{\sim}0.2\mu m$ |
|---|---|---|---|---|---|
| $dt{\sim}0.2ms$ | 1.6% | 3.5% | 7% | 14% | 30% |
| $dt{\sim}2\mu s$ | 1.6% | 3.5% | 7% | 14% | 30% |

The results for the two extreme discretizations in space and time reported in Table 9 are displayed in Figure 19 below. $j_v$ predictions are shown along with the experimental estimates; the model gives the right order of magnitude. No dependence on the time step below 0.2ms is found. No dependence on spatial discretization below $0.2\mu m$ is found for the numerical integration scheme. However, the numerical scheme fully converges to the analytical scheme for very small spatial step only, i.e. order of nanometers. Finally, we plot the figure of merit $\Delta$ as a function of time and discretization in Figure 20, which summarizes the above mentioned information.

The C++ routines implementing the microlayer evaporation subgrid model in TransAT are reported in Appendix A.

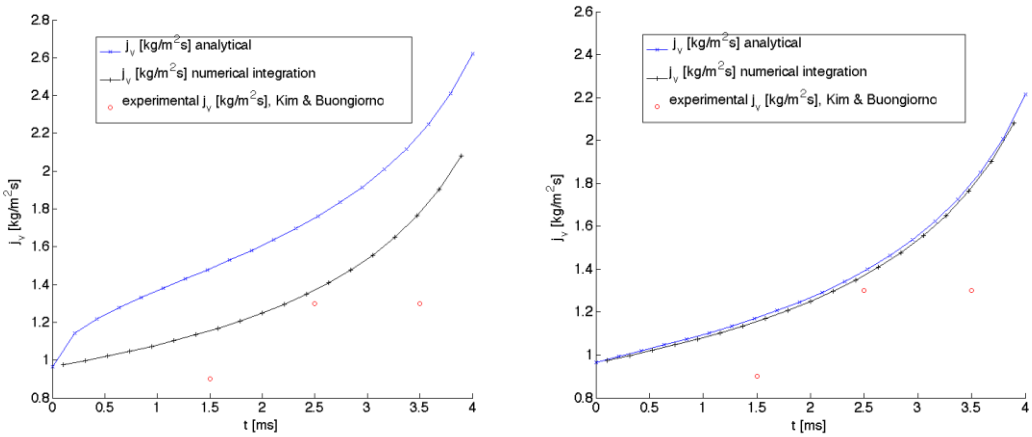


(a) (b)

Figure 19: Evaporative mass flux as a function of time, calculated from both analytical and numerical integration schemes, with (a) coarse spatial and time steps, dt=0.2ms and dr=200nm and (b) with refined spatial and coarse time steps, dt=0.2ms and dr=12.5nm.

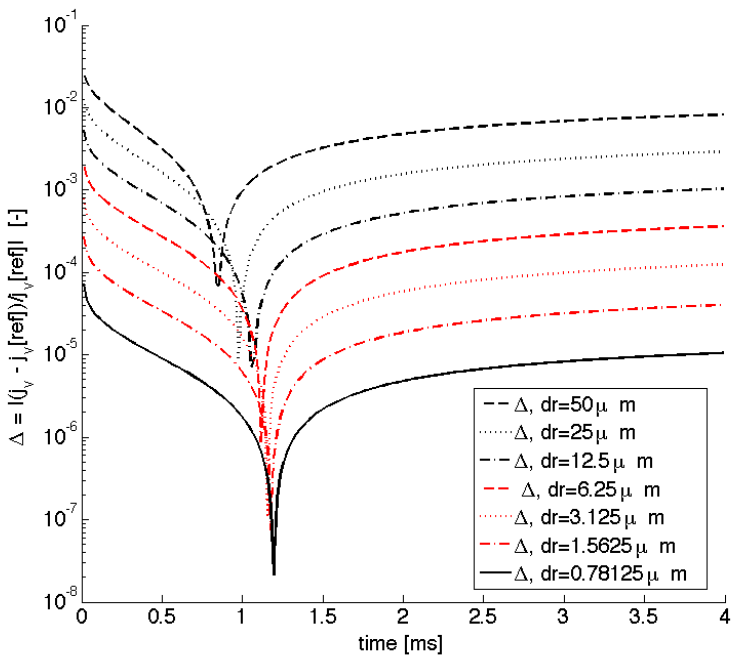


Figure 20: Time evolution of $\Delta$ for various spatial discretizations.

# 4 Growth and detachment of a single steam bubble from a wall at saturated pool boiling conditions (Test Case 3b)

## 4.1 Problem Formulation

The problem of a single vapor bubble growing off of a heated wall surrounded by superheated water is considered here. The physical situation is described in detail in the Test Case 3b report; however a short description is also given here. Conduction heat transfer increases the temperature of water near the wall and once the liquid reaches a superheat required to activate a nucleation site then a bubble starts forming and pushing the surrounding liquid outward. However, there is a thin liquid layer, known as the microlayer, that remains in contact with the wall underneath the bubble. Initially, bubble growth is driven by intense evaporation occurring both at the bubble interface and in the microlayer. When the size of the bubble becomes sufficiently large, buoyancy causes the bubble to detach from the wall. During this process there are several different modes of heat transfer depicted in Figure 21.

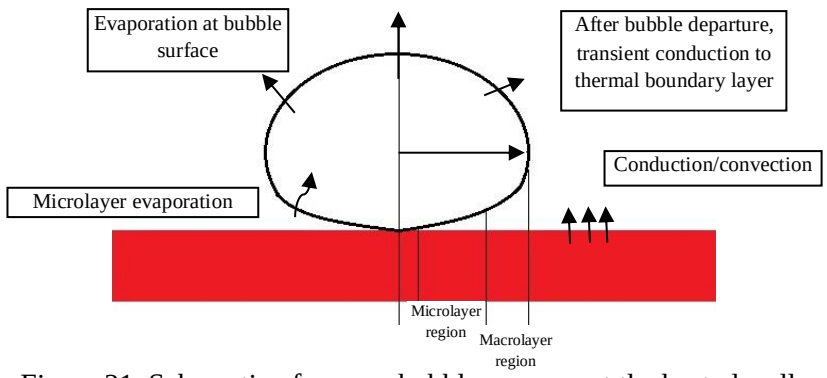


Figure 21. Schematic of vapour bubble growing at the heated wall.

The problem that is being simulated here is the numerical version of the nucleate boiling experiment performed in the MIT boiling facility. The experiment was conducted at atmospheric pressure, the bubbles generated were considered to be isolated from each other and the heated wall used consisted of a sapphire substrate and a thin heating layer on the top of it. The details for the experimental setup and data can also be found in the Test Case 3b report.

We here compare numerical results from TransAT simulations to experimental results for the Test Case 3b. For now the focus is on growth time (i.e. bubble departure time), measured to be ~14.7 ms, departure radius, measured to be ~1.85 mm, and bubble shape (see experimental data in Fig. 22).

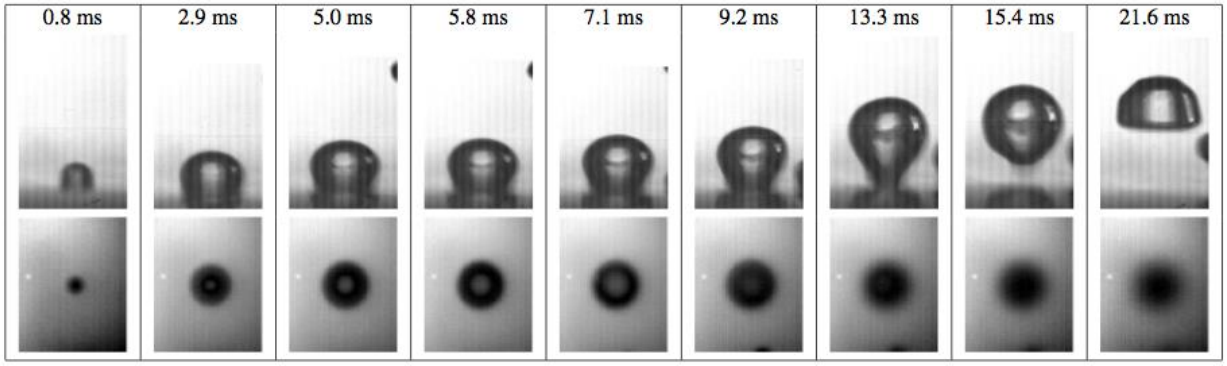

Figure 22: Synchronized high-speed video and infrared video of steam bubble at atmospheric pressure growing on a sapphire wall. The top sequence is a lateral view of the bubble; the bottom sequence is the two-dimensional temperature distribution on the sapphire surface underneath the bubble. The nucleation temperature for this bubble was ~109°C, the bubble departure occurred at about ~14.7 ms after nucleation with a departure radius of ~1.85 mm.

## 4.2 Numerical Simulations and Results

The code TransAT was used for the simulations reported here, which are 2D axisymmetric simulations of a sector of the bubble corresponding to an angle of 1 rad on the plane of the heater. The fluid and substrate properties used in the simulations are given in Table 10.

Table 10: Working fluid properties for nucleate boiling simulations with TransAT

| Properties | Water | Steam | Substrate |
|---|---|---|---|
| $\rho\ (kg/m^3)$ | 958 | 0.6 | 3970 |
| $\mu\ (Pa\,s)$ | 2.8e-4 | 1.2e-5 | - |
| $\lambda\ (W/mK)$ | 0.681 | 0.025 | 30 |
| $c_p\ (J/kgK)$ | 4218 | 2034 | 900 |
| $h_{lg}\ (J/kg)$ | 2.257e+6 | | |
| $T_{sat}\ (K)$ | 373.15 | | |
| $T_n\ (K)$ | 382.15 | | |
| $\sigma\ (N/m)$ | 0.059 | | |
| $g\ (m/s^2)$ | 9.81 | | |
| $R_o$ (μm) | 100 | | |
| $q''(kW/m^2)$ | | | 28.7 |

The test matrix for the simulations in FY13 aimed at identifying the effect of (i) using the newly-developed sharp-interface treatment for the energy equation and (ii) adding the microlayer contribution to bubble growth from the extended microlayer model presented in Section 2 above. The simulation domain is taken as 5 mm in the horizontal direction and 15 mm in the vertical direction. The test matrix is shown in Table 11. Three grids (Table 12) are studied for each case, to evaluate grid convergence.

Table 11: Test matrix for Test Case 3b simulations with and without micro-layer evaporation models

| Conjugate heat transfer | Contact angle | Microlayer model | Initial wall superheat | Planar heat generation rate |
|---|---|---|---|---|
| No | 80° | -- | 10°C | -- |
| No | 80° | Yes | 10°C | -- |
| Yes | 80° | -- | 10°C | 28.7 kW/m$^2$ |
| Yes | 80° | Yes | 10°C | 28.7 kW/m$^2$ |

Table 12: Discretization parameters for the nucleate boiling problem

| Grid | Minimum cell size (μm) | Actual discretization in nodes (z & r) |
|---|---|---|
| Coarse | 100 | 150x48 |
| Medium | 50 | 300x96 |

| | | |
|---|---|---|
| Fine | 25 | 600x192 |

### 4.2.1 Simulations with constant wall superheat

The results are reported in terms of bubble radius as a function of time in Figure 23. The simulations over predict the experimental bubble departure time due to underestimation of the mass-transfer rate. However, as expected the departure diameter is well predicted since it is a large scale phenomenon driven by a balance of buoyancy, surface tension and the mass-transfer rate.

Figure 23 shows the evolution of the bubble base diameter with time until the bubble detaches and leaves the upper boundary. The departure time reduces with grid resolution – the departure diameter remains more or less constant. An additional test with a more wetting contact angle shows that the departure time and diameter can considerably vary based on the contact angle. The evolution of the base radius of the bubble is presented in Figure 24. The departure time can be measured using this metric since at departure the triple line length goes to zero. The base radius reaches values between 1.8-2.0 mm. It appears that the constant wall temperature case should have departure radii greater than the real case with conjugate heat transfer. Animations for all the three cases are included in the *Supplementary Materials* presentation.

Simulations were also performed with the dynamic contact angle model available in TransAT (TransAT manual, 2013) for the case with constant wall superheat. The evolution of the base radius of the bubble and the effective diameter of the bubble is presented in Figure 25. It is seen that the effect of a dynamic contact angle model is not significant for the contact angle of $80^o$ used in the study. For the low contact angle of $38^o$ the bubble departure is much earlier.

Snapshots of the bubble growth stages are presented in Figure 26. It shows that the shape of the bubble obtained is qualitatively similar to that observed in the experiments. A quantitative comparison is only possible if both the departure diameter and the departure time of the bubble are accurately reproduced in the simulations. Note that the temperature inside the bubble goes above the saturation temperature due to direct heat conduction from the wall. This cannot be prevented, and is actually physically correct in the modeling since the wall temperature is fixed and on contact with the vapor heat flows into the vapor phase. However, due to the low heat capacity of the vapor, this does not impact the growth of the bubble.

Table 13 shows the departure diameters and departure times obtained for the cases with fixed wall temperature. The departure time converges with grid refinement, however the grid converged value has not yet been reached. With the results for the three grid resolutions, a more accurate estimate for the departure time can be obtained using Richardson's extrapolation. Note that the departure diameter for the fine grid is higher since some delay in departure was observed due to fine scale effects such as necking. It must be taken into account that the constant wall temperature case is different from any experimental setup since the wall is always hot and there is growth of the bubble even during the return phase of the bubble – which would not be the case in reality due to the cooling of the substrate.

Table 13: Discretization parameters for the nucleate boiling problem

| Grid | Departure time (ms) | Departure diameter (mm) |
|---|---|---|
| 1 | 340 | 4.875 |
| 2 | 202 | 4.853 |
| 3 | 131 | 5.22 |
| Richardson | 45 | -- |

| | | |
|---|---|---|
| extrapolation | | |

It is clear that a departure time of 14-15 ms, as observed in the experiment, cannot be obtained without the use of a micro-layer model. The departure time obtained with Richardson extrapolation (using first-order convergence of the departure time) is still 3 times higher than the expected departure time.

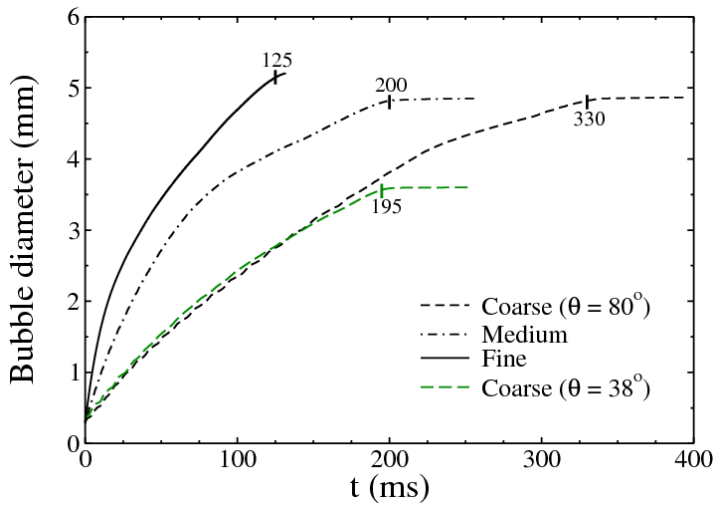


Figure 23: Bubble effective diameter as a function of time for the three grids (coarse, medium, fine) for the simulations without any micro-layer model for constant wall superheat.

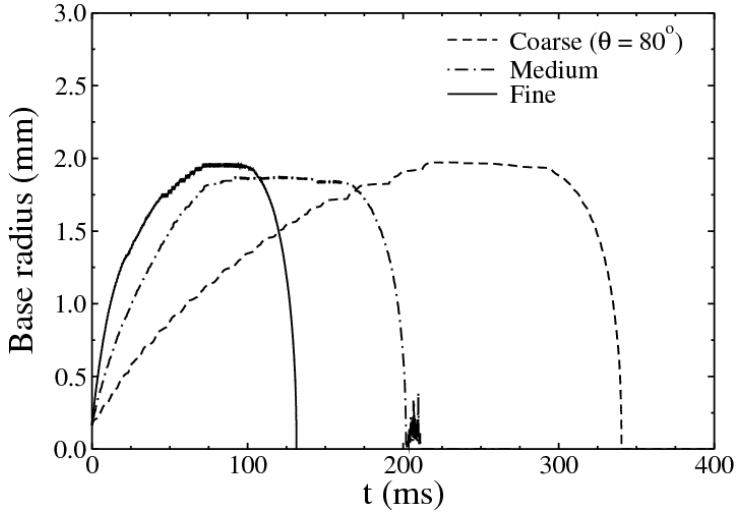


Figure 24: Bubble base radius as a function of time for the three grids (coarse, medium, fine) for the simulations without any micro-layer model for constant wall superheat.

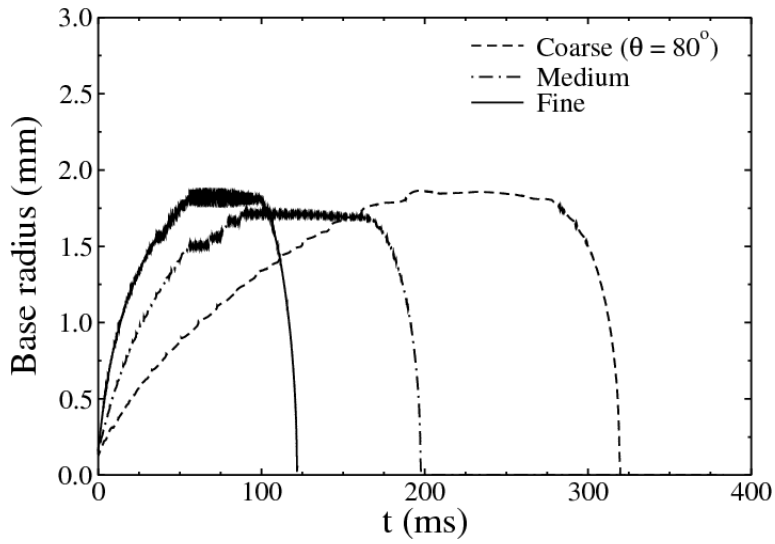


(a)

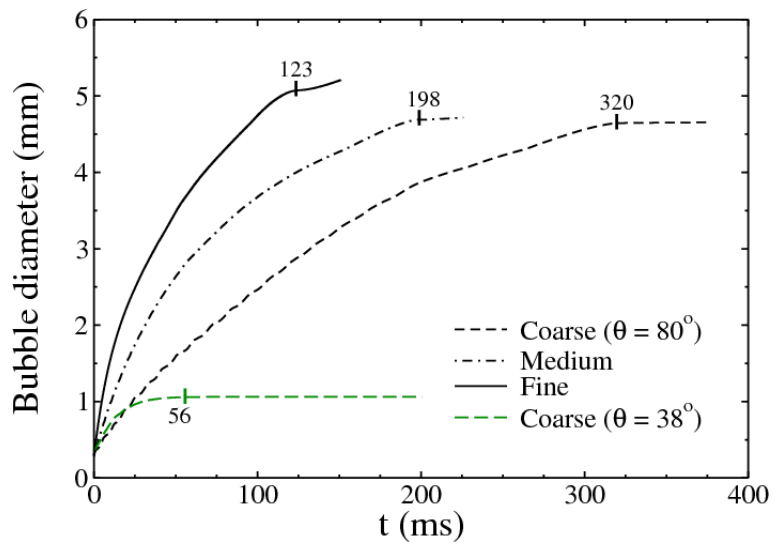


(b)

Figure 25: Evolution of the bubble base radius (a) and the bubble effective diameter (b) for the case with constant wall superheat using the dynamic contact angle model of TransAT

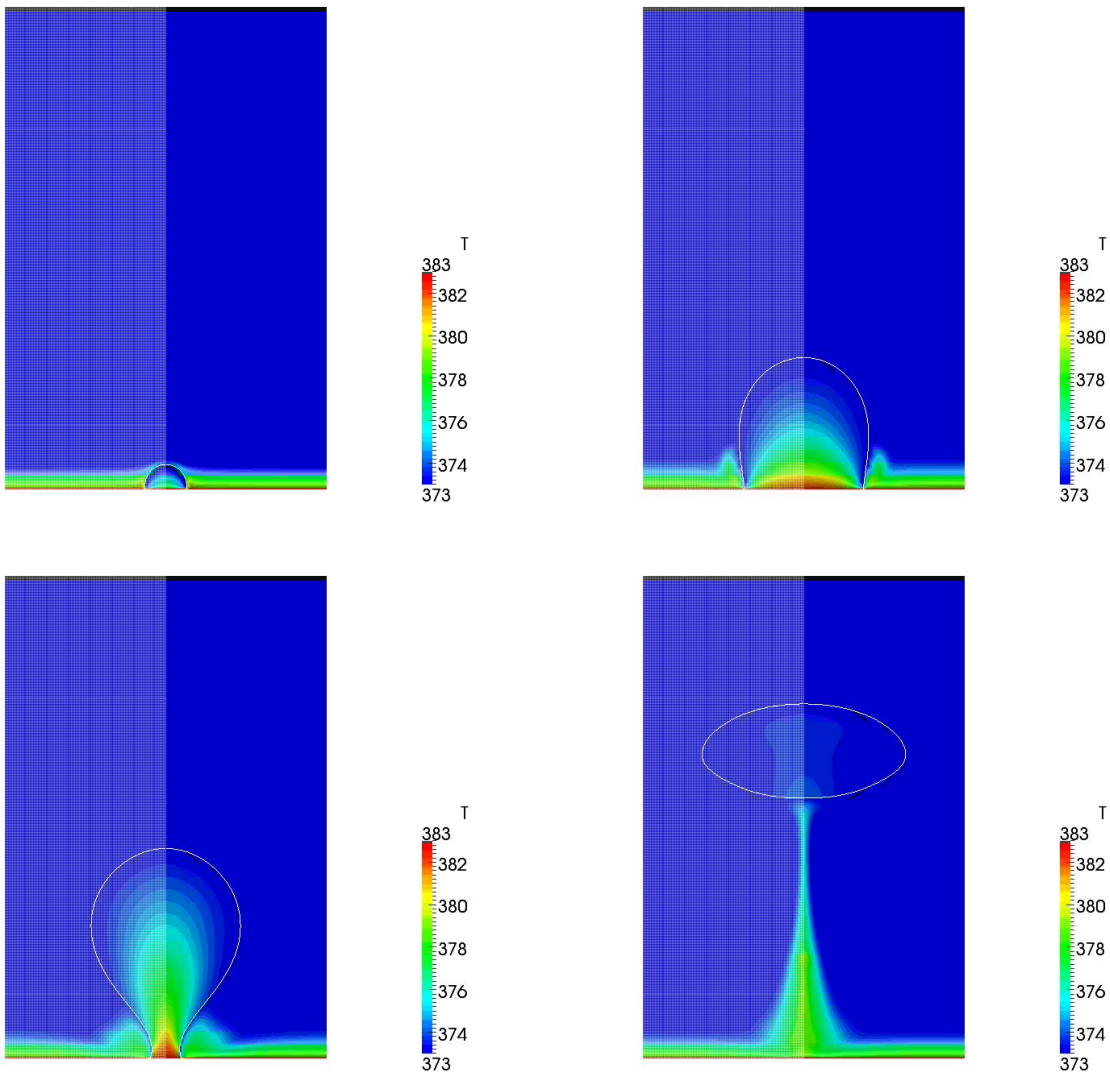


Figure 26: Snapshots of the evolution of the steam nucleate for a fixed wall superheat of 10 K (for medium grid). Note that due to adaptive time stepping the intervals between the images are not constant.

### 4.2.2 Simulations with conjugate heat transfer

Conjugate heat transfer simulations were run for the cases without the micro-layer model; not yet with the extended micro-layer model. For the conjugate heat transfer simulations, the immersed surface method of TransAT was used. For the immersed surface method to handle the strong phase change source term at the triple line a finer grid was used as the base case with slight grid stretching towards the center of the nucleate. Therefore only 2 grids were used – such that the grid resolution was equal to the Medium and Fine grids described in the previous section.

Table 14: Discretization parameters for the nucleate boiling problem

| Grid | Minimum cell size (µm) | Departure time (ms) | Departure diameter (mm) |
|---|---|---|---|
| 1 | 50 | 204 | 3.76 |

| | | | |
|---|---|---|---|
| 2 | 25 | 200 | 3.75 |

The bubble diameter evolution is presented in Figure 27 along with the evolution of the base diameter. A very different behavior as compared to the constant wall temperature can be observed. The bubble grows up to a certain base diameter (in this case approximately 1 mm), after which the bubble grows with a constant base diameter followed by a rapid departure. In contrast to the constant wall superheat case, the departure time does not strongly depend on the grid resolution. For the finer grid, the base radius reaches its highest value earlier but remains at this radius for a longer period of time. The reason for this could be the cooling of the substrate due to phase change which is not present in the constant wall superheat case. The departure diameters for the two grids are also very close ~ 3.75 mm, which is very close to the experimental result.

Snapshots of the evolution of the temperature field are shown in Figure 28. In comparison to the constant wall superheat case, the cooling of the substrate is clearly observable. On departure of the bubble, the substrate starts to heat up again. Once more, the departure time obtained without considering any micro-scale mass-transfer effects is too large compared to the experimentally observed time. Direct comparison of the heating period can only be undertaken when the departure time is well captured. Clearly, further work to include the micro-layer model presented in the preceding section is essential; such work is underway and the results form simulations including the microlayer will be reported in the near future.

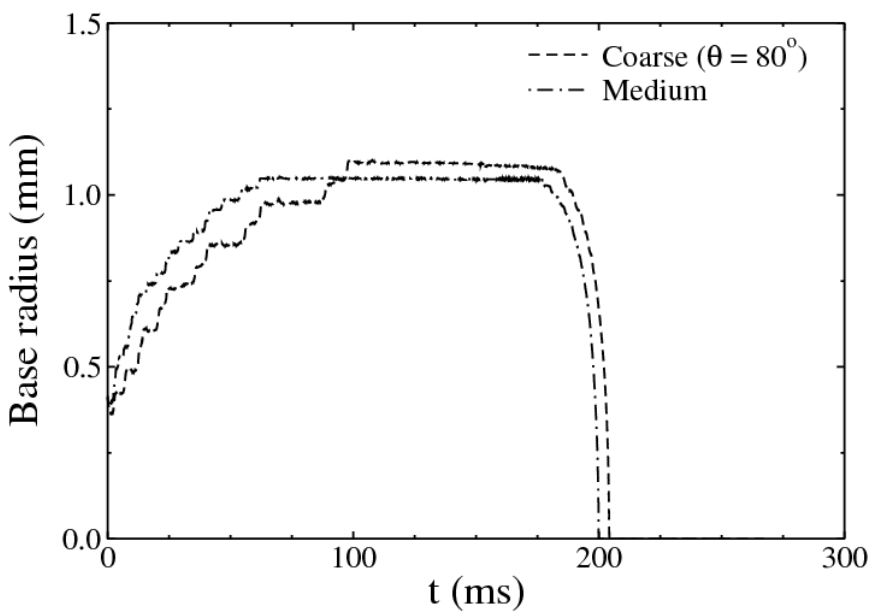

(a)

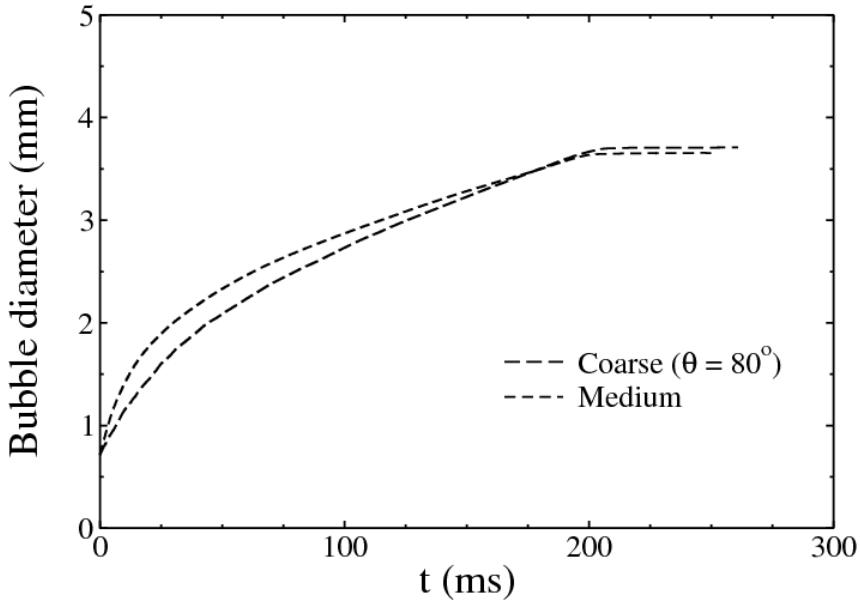


(b)

Figure 27: Evolution of the bubble base radius and the bubble effective diameter for the conjugate heat transfer case using the dynamic contact angle model of TransAT. Note: for the Immersed surface method only the dynamic contact angle model is available in TransAT.

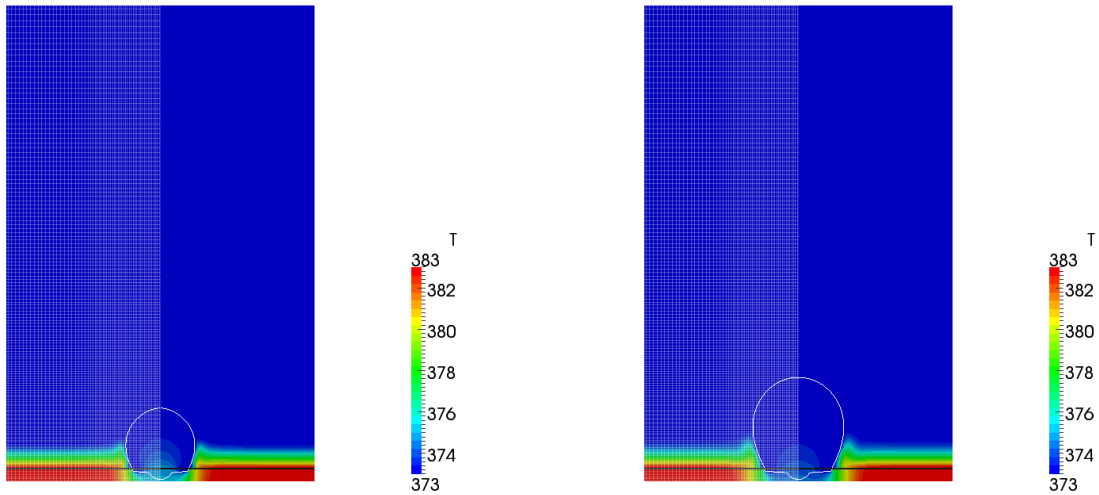

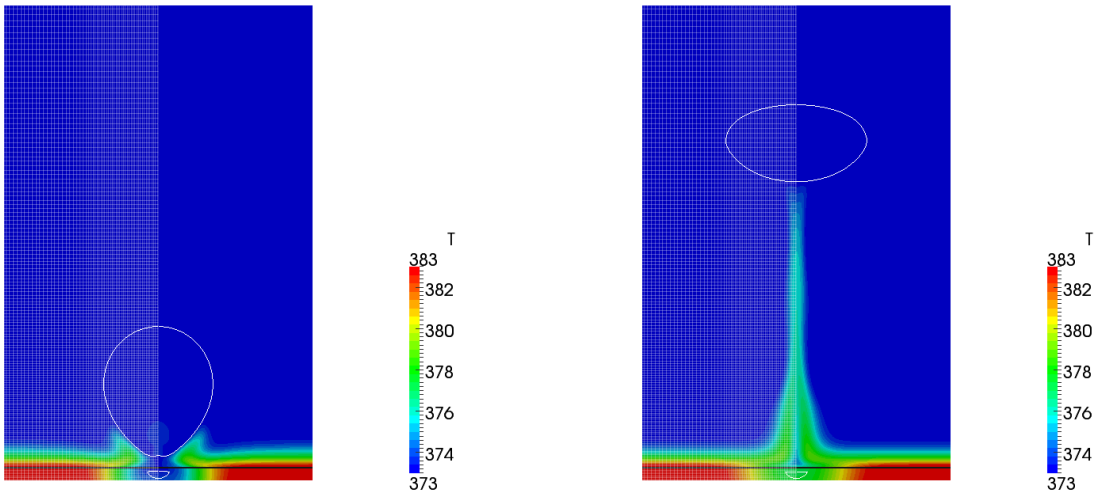


Figure 28: Snapshots of the evolution of the steam nucleate for the conjugate heat transfer case (for the coarser grid). Note that due to adaptive time stepping the intervals between the images are not constant.

### 4.2.3 Simulations with micro-layer model

The micro-layer subgrid model discussed in Section 2 was implemented in an external routine running with *TransAT*. Two approaches for modeling the outer-edge of the micro-layer were explored: set a maximum radial expansion of the micro-layer $r_{out} \leq 0.5$mm, as suggested by experimental observations, or limit the micro-layer region at any time step to the full base of the bubble, i.e.g. $r_{out} = R_{base}$. The initial shape of the micro-layer is assumed to be linear with a slope of 0.01 (typical) and an inner thickness of 1.7nm (typical thickness of the absorbed layer). The simulations of Test Case 3b impelemtning the microlayer model are underway and will be presented in the next revision of this report.

# 5 Conclusions and future work

The advanced phase-change model of TransAT based on a sharp-interface treatment of the energy equation in the level-set framework is capable of reproducing the analytical solutions of various simple benchmarks well. For the nucleate boiling benchmark, the bubble departure size is captured very well for the case with conjugate heat transfer. The departure time in all cases is too high compared to the experimental value of 14-16 micro seconds. A micro layer model has been shown to be essential for capturing the growth rate of the nucleate.

Future work should complete the Test Case 3b simulations to include the coupled models for the micro-layer and the conjugate heat transfer in the substrate. Sensitivity of the numerical solution to the assumed values of the contact angle and bubble nucleation temperature should be assessed. Repeated ebullition cycles should be simulated to achieve a cyclic steady state which does not depend on the initial conditions, i.e. initial temperature profile in the boundary layer above the wall. More exhaustive comparison of the numerical predictions to the experimental database, in terms of bubble shape and temperature profiles, should be carried out.

## References


- Alexiades, V. and A.D. Solomon, Mathematical Modeling of Melting and Freezing Processes. 1993, New York: Hemisphere, Washington DC.
- V. P. Carey, Liquid-Vapor Phase-Change Phenomena, Tay- lor and Francis, 2nd Ed., 2008.
- Gibou, F., et al., A level set based sharp interface method for the multiphase incompressible Navier–Stokes equations with phase change. J. Comp. Phys., 2007. 222: p. 536-555.
- Gupta, S.C., The Classical Stefan Problem: Basic Concepts and Analysis. Elsevier Science, 2003. Amsterdam.
- A. Guion, D. Langewisch, J. Buongiorno, "Dynamics of the liquid microlayer underneath a vapor bubble growing at a heated wall", HT2013-17174, *Proc. Summer Heat Transfer Conference*, Minneapolis, MN, July 14-19, 2013.
- Hardt, S. and F. Wondra, Evaporation model for interfacial flows based on a continuum-field representation of the source terms. Journal of Computational Physics, 2008. 227(11): p. 5871-5895.
- H. Kim and J. Buongiorno. Detection of liquid vapor solid triple contact line in two-phase heat transfer phenomena using high-speed infrared thermometry. *International Journal of Multiphase Flow*, 37(2):166–172, 2011.
- C. Kunkelmann , C., & Stephan , P. (2009 ). CFD simulation of boiling flows using the volume-of-fluid method within openfoam . *Numerical Heat Transfer, Part A: Applications , 56* , 631–646 .
- Magnini , M. (2012, May). CFD modeling of two-phase boiling flows in the slug flow regime with an interface capturing technique. Universita di Bologna .
- Mikic, B.B., W.M. Rohsenow, and P. Griffith, On bubble growth rates. International Journal of Heat and Mass Transfer, 1970. 13(4): p. 657-666.
- P. Stephan, J. H. (1994). A new model for nucleate boiling heat transfer. *Warme and Stoffubertragung, 30*, 119-125.
- Plesset , M., & Zwick , S. (1954). The growth of vapor bubbles in superheated liquids. *Journal of Applied Physics , 25*, 493–500 .
- Sato, Y. and B. Niceno, A New Conservative Phase Change Model for Nucleate Boiling, in 20th International Conference, Nuclear Energy for New Europe 2011. 2011: Bovec, Slovenia.
- Scriven, L. (1959). On the dynamics of phase growth. *Chemical Engineering Science, 10*, 1-13.
- P. Stephan, J. Hammer, A new model for nucleate boiling heat transfer, Warme and Stoffubertragung 30 (1994) 119–125.
- TransAT User Manual (2013) ASCOMP GmbH, Zurich, Switzerland.
- H. Wang, S. V. Garimella, and J. Y. Murthy. Characteristics of an evaporating thin film in a microchannel. Int. J. Heat Mass Transfer, 50(19-20):3933-3942 (2007).
- Welch, S.W.J. and J. Wilson, A Volume of Fluid Based Method for Fluid Flows with Phase Change. Journal of Computational Physics, 2000. 160(2): p. 662-682.

## APPENDIX – C++ routines for implementation of the microlayer subgrid model in TransAT

```
#include "userglobal.h"
#include "userglobal_prototype.h"
#include "user_interface.h"
#include "cppinterface.h"
#include <iostream>
#include <stdio.h>
#include <cmath>
#include <cstring>

UserGlobal::UserGlobal(){
  debug = 0;
}

UserGlobal::~UserGlobal(){
}

// every time step before solver
void UserGlobal:: User_processing_beforesolver() {
   int nijk=get_integer("nijk");
   int NI=get_integer("ni")   ;
   int NJ=get_integer("nj");
   int NIJ=NI*NJ;
   double time, dtime;
   double lambl, rhol, rhov, rholv, hfg;
   double *phi, *y, *x, *mdot, *ycor, *xcor;
   double *areagl;
   int timestep;
   int ii, i, j, k;

   timestep = get_integer("timestep");
   time   = get_double("time");
   dtime  = get_double("dtime"); //  check TransAT keyword for dtime

   //FLUID PROPERTIES
   lambl = get_double("lambl");
   rhol= get_double("rhol");
   rhov= get_double("rhog");
   rholv=rhol-rhov;
   hfg= get_double("latent");
   if (debug && timestep == 1) {
      fprintf(stderr,"lambl %f\n",lambl);
      fprintf(stderr,"rhol  %f\n",rhol);
      fprintf(stderr,"rhov  %f\n",rhov);
      fprintf(stderr,"rholv %f\n",rholv);
      fprintf(stderr,"hfg   %f\n",hfg);
   }
```

```
set_pointer(&phi ,"levelset");
set_pointer(&y   ,"cellcentery");
set_pointer(&x   ,"cellcenterx");
set_pointer(&ycor,"cellcornery");
set_pointer(&xcor,"cellcornerx");

set_pointer(&mdot  ,"mdot");
set_pointer(&areagl,"areagl");

//get bubble outer edge radius
double r_dry, r_bubble;
int ii_bubble;
ii=0;
i=2;
k=2;
for (j=2; j < NJ; j++) {
  ii = (i-1) + (j-1)*NI + (k-1)*NIJ;
  if (phi[ii]*phi[ii+NI] < 0) break;
}
ii_bubble=ii;
double phisum = fabs(phi[ii_bubble]) + fabs(phi[ii_bubble+NI]);
r_bubble = ( y[ii_bubble+NI]*fabs(phi[ii_bubble])
            +y[ii_bubble]   *fabs(phi[ii_bubble+NI]))/phisum;
fprintf(stderr,"ii_bubble %i %i\n",ii_bubble,j);
fprintf(stderr,"r_bubble  %f   \n",r_bubble);

//SIMULATION PROPERTIES
//initial microlayer linear shape properties
double d0, dou, dT0, rmax, s;
rmax = 0.99*r_bubble;
d0   = 1.7e-9;  // absorbed layer thickness
s    = 0.01;    //initial slope from r_dry = 0 to contact line
dT0  = 9.0;     // wall superheat to remain constant
dou  = d0 + s*rmax;  // outer edge thickness of initial
                     // microlayer (linear shape)

//UPDATE MDOT FOR ALL BOUNDARY CELLS
//mdot (need time and time+dtime)
//update mdot under the microlayer
double t1;
t1=time;

double rdry_t   = rdry(t1, d0, s, dT0, lambl, rhol, hfg);
double rinner, router;
double mdotii, dy, ymid;
double Vi, Vip;

//reset vector
microlayer.clear();
```

```
mdotarea triplet;
//Alex: we can also store the microlayer thickness just like
//      I am storing the mdot, area, ii triplet

ii=0;
i=2;
k=2;
for (j=2; j < NJ; j++) {
   ii = (i-1) + (j-1)*NI + (k-1)*NIJ;

   rinner = std::max(rdry_t,y[ii]);
   router = std::min(rmax,y[ii+NI]);

   dy   = router-rinner;
   ymid = 0.5*(router+rinner);

   double microarea = dy*ymid;
   double jv;

   if (y[ii+NI] >= rdry_t && y[ii] < rmax) {
      Vi =std::max(f_( rinner, router, s, time      , d0, dT0
                      ,lambl,rhol, hfg),0.);
      Vip=std::max(f_( rinner, router, s, time+dtime, d0, dT0
                      ,lambl,rhol, hfg),0.);
      if (debug && timestep == 1) {
         if (Vi  > 0.0) {fprintf(stderr,"Vi  %f\n",Vi *1.e12);}
         if (Vip > 0.0) {fprintf(stderr,"Vip %f\n",Vip*1.e12);}
      }

      jv = std::max(rhol/(microarea)*(Vi-Vip)/(dtime),0.); //kg/m2s
      mdot[ii]   = mdot[ii]   + jv;
      areagl[ii] = areagl[ii] + microarea;

      // Save the values of microlayer mdot and areas
      // for later use (temperature equation)
      triplet.index  = ii;
      triplet.mdot   = mdotii/microarea;
      triplet.areagl = microarea;
      microlayer.push_back(triplet);
   }
} //End Mdot

if (debug)
{
   printf("number of points in ML %i\n",microlayer.size());
   for (int i = 0; i < microlayer.size(); i++)
   {
      printf("index  %i \n",microlayer[i].index);
      printf("mdot   %e \n",microlayer[i].mdot);
      printf("areagl %e \n",microlayer[i].areagl);
```

```
      }
   }

}; //End Before Solver

void UserGlobal:: User_adjust_linear_system(char* varname)
{
   if (strcmp(varname,"temperature") == 0) {
      if (debug) printf("%s\n", varname);
      add_mdot_source_temperature();
   }

};

void UserGlobal:: add_mdot_source_temperature()
{
   double *tissu, *hembed, *tissp, *temp, *aw;
   double latent, tsat;
   int ii;
   double mdot, areagl, term;

   if (debug) printf("inside add_mdot_source_temperature\n");

   set_pointer(&tissu ,"issu");
   set_pointer(&tissp ,"issp");
   set_pointer(&hembed,"hembed");
   set_pointer(&temp  ,"temperature");
   set_pointer(&aw    ,"westcoeff");

   latent = get_double("latent");
   tsat   = get_double("tsat");
   if (debug)
   {
      printf("latent heat %e\n",latent);
      printf("Tsat        %e\n",tsat);
   }

   for (int i = 0; i < microlayer.size(); i++){
      ii     = microlayer[i].index;

      //// for conjugate heat transfer problem
      //mdot   = microlayer[i].mdot;
      //areagl = microlayer[i].areagl;
      //term   = hembed[ii]*mdot*areagl*latent;
      //// mdot is assumed to be positive
      //tissp[ii] = tissp[ii] - term/temp[ii];

      // for constant wall temperature case
      // just set the temperature to be Tsat
```

```
      temp[ii]  = tsat;
      tissp[ii] = -1.0e+24;
      tissu[ii] = 1.0e+24*tsat;
   }
};
```

XXXXXXXXXXXXXXXXXXXXXXXXXXXXXXXXXXXXXXXXXXXXXXXXXXXXXXXXXXXXXX

```
#include<stdio.h>
#include <math.h>
#include "userglobal.h"
#include "userglobal_prototype.h"

#define PI 3.14159

double UserGlobal::f_(double rin,double rout,double s, double t,
double d0, double dT0, double k, double rhol, double hfg)
{
int N=25;
int NN=N-1;
int ii;
double vol=0.;
double volf=0;
double rip, ri, dip, di;
for(ii=1;ii<=NN;ii++){
  ri=rin+(ii-1)*(rout-rin)/(N-1);
  rip=rin+ii*(rout-rin)/(N-1);
  dip=fmax(g_(rip, s, t, d0, dT0, k, rhol, hfg),d0);
  di=fmax(g_(ri, s, t, d0, dT0, k, rhol, hfg),d0);
  vol=vol+PI/2.*(rip+ri)*(dip+di)*(rip-ri);
}
volf=vol;
return volf;
}
```

XXXXXXXXXXXXXXXXXXXXXXXXXXXXXXXXXXXXXXXXXXXXXXXXXXXXXXXXXXXXXXXX

```
#include<stdio.h>
#include <math.h>
#include "userglobal.h"
#define PI 3.14159

double UserGlobal::g_(double r,double s, double t, double d0, double
dT0, double k, double rhol, double hfg)
{
return sqrt((d0+s*r)*(d0+s*r)- 2.*k*dT0*t/(rhol*hfg));
}
```

XXXXXXXXXXXXXXXXXXXXXXXXXXXXXXXXXXXXXXXXXXXXXXXXXXXXXXXXXXXXXXXXXX

```
#include<stdio.h>
#include <math.h>
#include "userglobal.h"
#define PI 3.14159

double UserGlobal::rdry(double t, double d0, double s, double dT0,
double k, double rhol, double hfg)
{

//return (rout/dout)*(pow(2.*k*dT0*t/(rhol*hfg),0.5)-d0);
return d0/s*(sqrt(1.+2.*k*dT0*t/ (rhol*hfg*d0*d0))-1.);
}
```